Myeloid cells contribute to bystander CD8 T cell accumulation in metabolic-associated steatohepatitis and are sufficient for fibrosis

Short title: Scar-associated macrophages fuel the immune-fibrosis niche

Authors

Cynthia Lebeaupin*[1], Katelyn L. Donahue*[1], Samir Lal[1], Stephen M. Christensen[1], Shoh Asano[1], Marc H. Wadsworth II[1], Kathryn Bound[1], Saurav De[1], James McMahon[2], Franklin Schlerman[1], Chang Wang[1], Xiao Chen[1], Alexander M.S. Barron[1], Thomas A. Wynn[1], Kevin M. Hart[1], Thomas Fabre[1]

Affiliations

[1] Pfizer Inc., Cambridge, MA, USA.

**These authors contributed equally to this work as first authors.*

Corresponding author

Thomas.Fabre@pfizer.com

1 Portland Street, Cambridge MA, USA

Keywords

MASH, fibrosis, scar-associated macrophages, CXCR6/CXCL16

Graphical abstract

The immunopathological niche in fibrosis

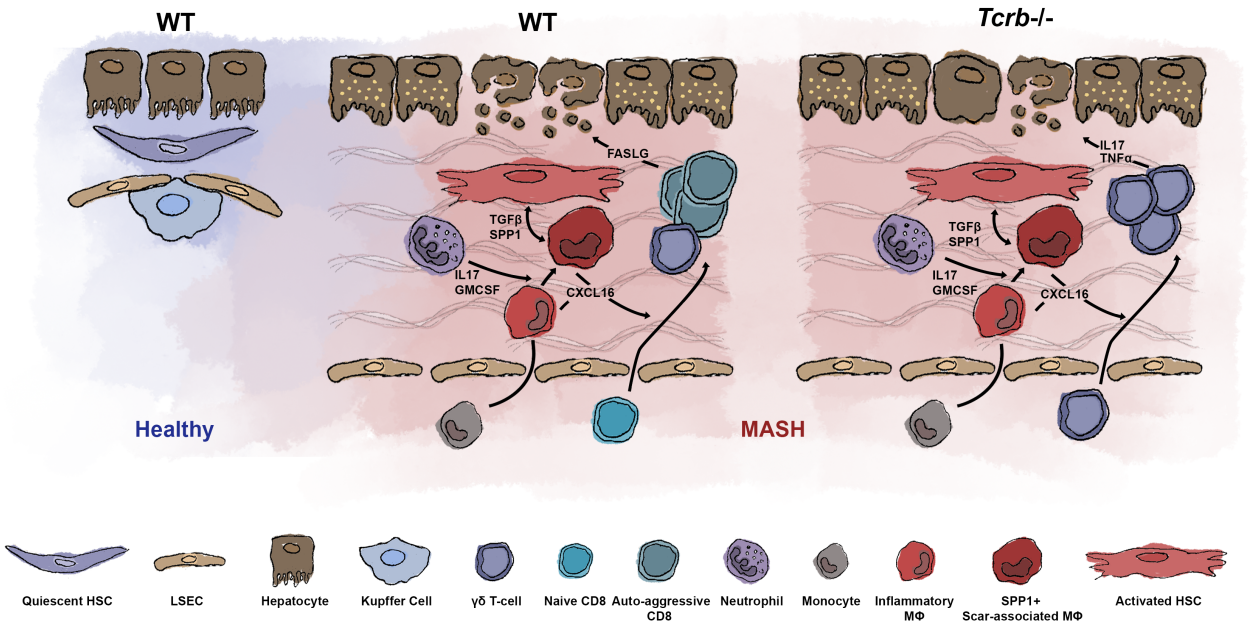

Highlights

- Adaptive and innate immune cells localize to the human MASH fibrotic niche
- CD8 T cells increase with MASH severity while MHC-II^{+} cells accumulate with fibrosis
- CXCR6^{+}FASLG^{+} CD8 auto-aggressive T cells accumulate at the scar
- CXCL16^{+} scar-associated macrophages retain CD8 T cells in the fibrotic MASH niche
- Liver injury, inflammation and fibrosis persist in the absence of conventional T cells

Impact and implications

Metabolic dysfunction-associated steatohepatitis (MASH) is a progressive liver disease in which fibrosis is a key determinant of patient outcomes and survival. This study demonstrates that fibrosis in MASH can develop independent of conventional T cell immunity, driven by myeloid cells including scar-associated macrophages (SAMs) and neutrophils within a localized hepatic niche in mice and humans. This highlights the need to prioritize innate immune mechanisms as key drivers of chronic (late-stage) liver disease for researchers and clinicians developing anti-fibrotic therapies.

Abstract

Background & Aims: Metabolic dysfunction-associated steatohepatitis (MASH) is a leading cause of liver fibrosis, morbidity, and mortality. It is characterized by the accumulation of fat in hepatocytes causing cell death followed by stromal cell activation and scar deposition at later disease stages. While a marked accumulation of cytotoxic CD8 T cells is observed in MASH in humans and mice, the role of adaptive immune cells in fibrosis progression remains debated.

Methods: Transcriptional data were curated from human datasets and preclinical mouse models, including mice deficient in TCRαβ T cells (*Tcrb*$^{-/-}$), which lack conventional CD4 helper and CD8 cytotoxic T cells, in diet-induced fibrosing MASH for single-cell RNA-sequencing. Specific human and mouse liver transcriptomic immune signatures were corroborated by flow cytometry and immunofluorescence.

Results: MASH was associated with the expansion of lymphocytes and myeloid cells. Auto-aggressive CXCR6^{+}PD1^{+}FASLG^{+} CD8 T cells were enriched in livers of high-fat-diet-fed mice and correlated with MASH and fibrosis. Notably, *Tcrb*-deficient mice in a chemical and dietary preclinical MASH model developed fibrosis to the same extent as wild-type mice and exhibited exacerbated pro-fibrotic type 3 inflammation. Loss of conventional CD8 T cells neither impacted myeloid cell number nor phenotype within the fibrotic niche. Neutrophil- and non-conventional lymphocyte-derived GM-CSF and IL-17A were central drivers in the fibrotic niche composed of pathogenic macrophages and activated myofibroblasts. Furthermore, myeloid cells were identified as the main source of CXCL16 in diseased livers, retaining auto-aggressive CD8 T cells to the scar and contributing to their accumulation. Thus, non-adaptive cells, including scar-associated macrophages (SAMs) and myofibroblasts, are sufficient for MASH-driven fibrosis in this model.

Conclusions: Targeting myeloid cells and fibroblasts should be prioritized as anti-fibrotic therapies for MASH.

66 **Introduction**

67

68 Fibrosis in metabolic dysfunction-associated steatohepatitis (MASH) represents a critical and
69 unresolved clinical challenge of chronic liver disease that will continue to rise over the next three
70 decades[1]. While recent advances in metabolic therapies show promise in reducing steatosis and
71 hepatocellular injury, fibrosis often persists[2,3]. MASH with fibrosis perpetuates due to a conserved,
72 self-perpetuating cycle of injury, inflammation, cell differentiation, and scarring[4]. A critical factor in
73 fibrotic progression and maintenance is the initiating inflammatory cascade. This involves the
74 recruitment and differentiation of innate immune cells (*e.g.,* monocytes to macrophages,
75 neutrophils) as well as the recruitment and activation of adaptive immune cells (*e.g.,* T cells),
76 leading to the establishment of a complex fibrotic niche[4].

77

78 Historically, the role of adaptive immunity in fibrosis has been contentious due to discrepancies
79 between preclinical models and human diseases. The involvement of adaptive immune cells (*e.g.,*
80 T and B cells) in viral hepatitis (HBV, HCV) and auto-immune hepatitis in humans is evident[5-10].
81 Auto- or viral-antigen-specific adaptive cells contribute to hepatocellular damage and activation
82 of myofibroblasts via both cytokine secretion and canonical cell death mechanisms (*e.g.,*
83 perforin/granzyme)[11-14]. In contrast, preclinical studies using carbon tetrachloride (CCl_4) or
84 dimethylnitrosamine (DMN)-induced liver injury in SCID and NOD/SCID mice demonstrated that
85 adaptive immunity was dispensable for fibrosis development[15,16]. However, the hepatotoxicity and
86 non-physiological mode of acute “sterile” chemical preclinical injury, such as CCl_4 and DMN, limits
87 the translational relevance and support of these findings. Moreover, the absence of adaptive
88 immunity in these settings may have altered the kinetics and quality of innate immune responses.
89 Despite these limitations, these foundational studies laid the groundwork for a broader
90 understanding of fibrosis as a maladaptive wound-healing response, potentially uncoupled from
91 classical adaptive immune pathways[17]. In the context of MASLD/MASH, perceived originally as a

92 “sterile” injury, more recent studies reported the expansion of Th2, Th17, Tregs and CD8 T cells
93 in liver biopsies, potentially resulting from dysbiosis and inflammation related to the peripheral
94 metabolic syndrome[11,18,19].
95
96 Investigations of adaptive immunity using diet-induced preclinical MASH models benefit from a
97 more organic, less “sterile” injury setting. In methionine and choline-deficient diet (MCDD)-
98 induced MASH, the ablation of $XCR1^+$ dendritic cells (DCs) decreased T cell activation and
99 reduced liver injury in mice[20]. In another report, choline-deficient high-fat diet (CDHFD) induced
100 the metabolic activation of CD8 T cells and NKT cells that promoted liver damage and MASH[19].
101 Recently, auto-aggressive $CXCR6^+PD1^+FASLG^+$ CD8 T cells that activate in response to calcium
102 influx rather than antigen recognition were shown to accumulate in high-fat diet- (HFD)-driven
103 MASH as well as human fibrotic livers. These auto-aggressive CD8 T cells exhibit transcriptional
104 profiles reminiscent of pathogenic T cells in chronic inflammatory diseases and mediate
105 FAS/FASLG-induced epithelial cell death[21]. However, these HFD models only showed modest
106 fibrosis induction and limited human validation. Furthermore, the contribution of auto-aggressive
107 T cells to fibrosis remains correlative, as the focus was on the composite non-alcoholic fatty liver
108 disease (NAFLD) activity score (NAS) and hepatoxicity, and the extent to which they are
109 necessary or sufficient for fibrogenesis remains unaddressed. Thus, while recent findings
110 implicate adaptive immunity in shaping hepatic inflammation, they fall short of establishing a
111 causal role in fibrosis progression.
112
113 Here, the role of conventional T cell-mediated adaptive immunity in the fibrotic niche was
114 interrogated by leveraging transcriptional and spatial profiling of human liver samples and
115 genetically modified mice lacking αβ T cells (*Tcrb-/-*) in a western diet-induced model of fibrosing
116 MASH. The findings of this study demonstrate that αβ T cells, while abundant in fibrotic tissue,
117 are not required for fibrosis progression. γδ T cells, with either an auto-aggressive-like or IL-17A

118 and TNFα phenotype, compensated in the absence of conventional T cells. Notably, the “core” of
119 the fibrotic niche appears to be independent of T cells and results from a myeloid-centric program
120 involving SPP1^{+} scar-associated macrophages (SAMs) and neutrophils that recruit CXCR6^{+} αβ
121 and γδ T cells and promote myofibroblast activation. These results challenge prevailing
122 assumptions about the immunological hierarchy in fibrosis and underscore the need to prioritize
123 innate immune mechanisms as therapeutic targets in chronic liver fibrotic disease.

Material and methods

Mouse strains and models

All procedures performed on animals were in accordance with regulations and established guidelines, which were reviewed and approved by an Institutional Animal Care and Use Committee and an ethical review process. All experimental procedures were performed at Pfizer (Cambridge, MA). C57BL/6J (WT) and *Tcrb*-/- (strain: 002118; The Jackson Laboratory, Bar Harbor, ME) male mice, starting at 6 weeks of age, were used for chemical (carbon tetrachloride; CCl_4) and/or diet-induced preclinical MASH (n= 6-15 per group). The mice were maintained in a thermo-neutral environment at a temperature of 30°C, humidity of 30-70%, and a 12 h-light/12 h-dark photocycle. Mice were injected with vehicle (olive oil) or CCl_4 (Sigma; 56-23-5 2x/week at 2 µl CCl_4/g) and/or fed a choline-deficient diet (CDA; Research Diets; A06071302) or HFD (Kcal of 40% fat, 20% fructose, and 2% cholesterol; D09100310; Research Diets, New Brunswick, NJ) for up to 40 weeks. Mice were euthanized using 5% CO2. Control animals were maintained on normal chow diet.

Human tissue sections

Human paraffin-embedded (FFPE) tissue sections were obtained anonymized from BioIVT with written informed consent. An institutional review board or independent ethics committee reviewed and approved relevant study documents, including the protocol. Study conduct adhered to the ethical guidelines of the 1975 Declaration of Helsinki principles, the Council for International Organizations of Medical Sciences international ethical guidelines, and all applicable laws and regulations. Human liver tissue samples sourced from vendors followed protocols that were reviewed and approved by appropriate regulatory and ethics committees. Patient metadata is available in Table S1.

150 **Tissue processing**

151 Livers from mice were collected on ice in cold RPMI 1640 medium, minced with a razor blade,
152 and collagenase-digested (100 U/ml; Sigma-Aldrich), shaking at 37°C for 1 h. After digestion, liver
153 tissues were filtered through 70 μm nylon mesh. Hepatocytes were removed by slow
154 centrifugation (50 g for 5 min) and non-parenchymal cells were enriched by centrifugation through
155 a 25% Percoll (GE Life Sciences) gradient at 850 g for 15 min. Erythrocytes were lysed with
156 ammonium-chloride-potassium buffer (Thermo Fisher Scientific). Cells were subsequently
157 distributed either for flow cytometry, restimulation with PMA/Ionomycin, or scRNA-seq.

158

159 **Multiplex cytokine analysis**

160 Intrahepatic leukocytes (IHLs) were resuspended at a concentration of 5 million cells per ml in
161 RPMI with 10% fetal bovine serum (FBS) and 1× stimulation cocktail (eBioscience) for 18 h.
162 Supernatants were collected and stored at -80°C. Multiplex cytokine/chemokine quantification
163 was performed using 25 μl of supernatant post-stimulation (LEGENDplex; BioLegend). Analysis
164 was performed using BioLegend Cloud analysis software. Data were expressed as fold change
165 normalized to control, chow-fed mice.

166

167 **Flow cytometry**

168 Mouse and human cells were washed with phosphate-buffered saline (PBS) and stained for 20
169 min at room temperature with LIVE/DEAD fixable aqua viability dye (Invitrogen). Cells were
170 washed with fluorescence-activated cell sorting (FACS) buffer and subsequently fixed with
171 Foxp3/Transcription Factor Fixation/Permeabilization buffer (Invitrogen). After washing
172 (PermWash Buffer; Invitrogen), cells were resuspended in freezing solution (90% FACS
173 buffer/10% dimethyl sulfoxide (DMSO)) and stored at -80°C. Once thawed, cells were washed,
174 and Fc receptors were blocked with TruStain FcX (mouse or human, as appropriate; BioLegend)
175 before staining with antibodies from Table S2. Cells were then washed, filtered through 60 μm

176 mesh, and run on a BD FACSymphony flow cytometer (BD). Data were analyzed with Omiq.ai,
177 using a DownSample and UMAP (Uniform Manifold Approximation and Projection) workflow.
178
179 **cycIF staining and analysis**
180 Human and mouse cyclic immunofluorescence (cycIF) was performed as described[22,23], using
181 antibodies listed in Tables S3 or S4, respectively . Briefly, human or mouse liver FFPE sections
182 were deparaffinized, rehydrated, and subjected to heat-induced (Citrate PH 6) epitope antigen
183 retrieval. Slides were stained at 4°C overnight with primary antibodies in blocking buffer solution
184 (PBS, 0.05 % Tween-20, 5% bovine serum albumin, 0.1% Triton X-100). After three washes (PBS,
185 0.05% Tween-20), slides were stained with fluorescently conjugated donkey secondary antibodies
186 (diluted 1:500 in blocking buffer) for 1 h at RT. Slides were again washed, DNA-stained with 4′,6-
187 diamidino-2-phenylindole (DAPI; Invitrogen), and mounted in EverBrite Trueblack mounting
188 medium to reduce auto-fluorescence. Acquisition was performed on an Axioscan Slide Scanner
189 (Zeiss). Following imaging, coverslips were removed and antibodies were stripped for subsequent
190 rounds of staining. For image processing, acquired images were first subjected to shading
191 correction and stitching using the Zeiss ZEN blue DESK (version 3.0) image processing software.
192 Alignment across subsequent rounds was performed on their respective nuclear (DAPI) channel
193 in QuPath by applying the transformation to the remaining channels[24,25]. The multichannel image
194 pyramid was generated using Bioformats2Raw and Raw2OMETiff programs (Glencoe Software,
195 Seattle, WA) and before conversion into FCS for analyses in Omiq.ai.
196
197 **Fibrosis histology**
198 FFPE sections were deparaffinized and incubated for 30 min in Picro Sirius Red fast green
199 solution (Direct Red 81 0.2%, FCF 0.1% in 1.3% picric acid solution, Sigma-Aldrich). Sections
200 were vigorously rinsed in dH_2O, dried, mounted with Permount (Thermo Fisher Scientific), and
201 acquired on an Axioscan Slide Scanner (Zeiss) in brightfield and with polarized light.

202

203 **TUNEL staining**

204 Cell death was assessed using the ApopTag Peroxidase *In Situ* Apoptosis Detection Kit (Millipore-
205 Sigma, S7101), following the manufacturer's instructions. Briefly, mouse liver FFPE sections were
206 deparaffinized, pretreated with proteinase K and quenched with endogenous peroxidase followed
207 by the addition of equilibration buffer directly on each specimen. Slides were incubated with TdT
208 enzyme in a humidified chamber at 37°C for 1 h, washed, and an anti-digoxignenin conjugate was
209 applied to the slides kept in a humidified chamber for 30 min at room temperature. After additional
210 PBS washes, peroxidase substrate developed the color, slides were washed, and a methyl-green
211 counterstain was applied. Specimens were dehydrated with xylene and slides mounted with
212 Permount. Brightfield slide images were acquired on an Axioscan Slide Scanner (Zeiss) and
213 TUNEL-positive staining was quantified in QuPath.

214

215 **Immuno-histochemistry**

216 FFPE slides were deparaffinized, rehydrated, and subjected to antigen retrieval as described
217 above for cycIF. Endogenous peroxidases were quenched for 15 min at RT with 0.6% H_2O_2 in
218 MeOH. Slides were washed three times (dH_2O x2 followed by PBS x1), then incubated overnight
219 in a humidified chamber in blocking buffer solution with anti-CD3e (Abcam, Rabbit host, cat#
220 ab16669 and Invitrogen, Rat host, cat# MA5-16622, both 1:50) at 4°C. The following day, slides
221 were washed with PBS three times and then incubated for 45 min at RT with biotinylated
222 secondary antibodies (Goat anti-Rabbit IgG, Invitrogen, cat#65-6140 and Goat anti-Rat IgG,
223 Vector Laboratories, cat#BA-9401-.5) diluted 1:300 in blocking buffer. The Vectastain Elite ABC
224 Kit, Peroxidase (Vector Laboratories, cat#PK-6100) was applied following the manufacturer's
225 protocol for 30 min at RT. Slides were developed for ~20 min using the DAB Substrate Kit
226 Peroxidase (Vector Laboratories, cat#SK-4100). Slides were washed in dH_2O and counterstained
227 with Modified Mayer's Hematoxylin (Epredia, cat#72804) for 2 min at RT. Slides were rinsed in

228 dH_2O and PBS sequentially and then dehydrated in 95% EtOH for 10 sec x2, 100% EtOH for 2
229 min x2, and xylene for 2 min x2 before mounting with Permount and drying overnight prior to
230 brightfield imaging on an Axioscan Slide Scanner (Zeiss).
231
232 **Mouse scRNA-seq and data analyses**
233 Cells from murine tissues were dissociated as described above, fixed in methanol following the
234 10X Genomics fixation protocol, and stored at -80°C (10X Genomics, Pleasanton, CA). A 3'
235 sequencing library was generated following protocols from 10x Genomics Single cell version 3.1.
236 Samples from WT animals were sequenced on an Illumina NextSeq 2000. Samples from the *Tcrb*-
237 /- animals were lipid-hashed as described[26] and sequenced on an Illumina NextSeq 500. FASTQs
238 were preprocessed and aligned with Cell Ranger version 8.0.1 using the mouse reference
239 GRCm39-2024-A. Downstream processing of count matrices was performed using Seurat version
240 5.1.0[27] and R version 4.4.0. Ambient RNA was corrected using SoupX version 1.6.2[28]. Samples
241 with lipid hashing were demultiplexed according to the Seurat workflow using HTODemux[29] with
242 positive.quantile = 0.95. Wild-type (WT) and *Tcrb*-/- samples were merged and subjected to QC
243 assessment using the Add_Cell_QC_Metrics functionality from scCustomize version 3.0.1
244 (RRID:SCR_024675, https://zenodo.org/records/17575311). Following uniform filtration, samples
245 were split into WT and *Tcrb*-/- groups and analyzed in parallel following the Seurat workflow with
246 the following modifiactions. Data were normalized with SCTransform with vars.to.regress =
247 "nCount_RNA"[30]. PC utilization was determined by assessing both the number of dimensions that
248 capture ~90% variance and the point at which change in variation between PCs became <0.1%.
249 Cells of interest (lymphocytes and myeloid cells) were subset from global objects, renormalized
250 and clustered as described above, and filtered for contaminating cell types. Gene signature
251 visualization was done with Nebulosa version 1.14[31].
252
253

254 **Deconvolution with BayesPrism and immune cell signature analysis**

255 Pre-processed scRNA-seq data of all cells from study GSE192742 were obtained from the
256 cellxgene initiative (https://cellxgene.cziscience.com/collections/74e10dc4-cbb2-4605-a189-
257 8a1cd8e44d8c) and pre-processed raw RNA-seq counts were obtained from GEO for study
258 GSE135251. *CD8A* and *CD4* expression was used to identify CD8 T and CD4 T cells in the T cell
259 cluster respectively using Seurat package[32]. To understand the cellular composition in samples
260 from healthy donors and patients with NAFLD and NASH, we applied BayesPrism[33] to predict the
261 abundance of cell types by modeling gene expression levels through bulk RNA-Seq data. Input
262 into BayesPrism included the raw counts from the bulk tissue and scRNA-seq normalized counts
263 from GSE192742 as a reference. Predicted cell type specific expression from BayesPrism was
264 normalized using variance stabilizing transformation using DESeq2 package[34]. Immune and
265 Kupffer cell gene sets were scored in the raw counts from the bulk tissue using the z-score method
266 in the hacksig package[35]. We applied linear regression to evaluate the association between
267 abundances of cell types, counts per million (CPM) of select genes and cell signature scores with
268 endpoints including age, histopathological stage and grade adjusting for batch and center as
269 covariates.

270

271 **Hydroxyproline quantification**

272 Liver and lung hydroxyproline content was quantified as previously described[11]. Tissues (100 to
273 200 mg) were hydrolyzed in 1 ml of 6 N HCl at 110°C overnight. Ten microliters of the hydrolyzed
274 sample or standard were placed in 30 µl of citric acetate buffer [10 g of citric acid (5%, w/v), 2.4
275 ml of glacial acetic acid (1.2%, v/v), 14.48 g of sodium acetate (7.24%, w/v), and 6.8 g of sodium
276 hydroxide (3.4%, w/v) with a total volume of 200 ml made up with sterile deionized water]. One
277 hundred microliters of chloramine T solution (0.282 g of chloramine T, 2 ml of isopropanol, 2 ml of
278 sterile water, and 16 ml of citrate acetate buffer) were mixed with the samples or standards and
279 oxidized for 20 min at room temperature. Oxidized samples or standards received 100 µl of

280 Ehrlich's reagent (2.5 g of *p*-dimethylaminobenzaldehyde, 9.3 ml of isopropanol, and 3.9 ml of
281 70% perchloric acid) and incubated at 65°C for 20 min. Optical density at 550 nm was recorded
282 and compared with the standard curve for quantification.
283
284 **Statistical analysis**
285 Statistical tests were conducted using R v4.4.0 (https://r-project.org/) or GraphPad Prism v10
286 (GraphPad Software, La Jolla, CA). Testing for differential expression was performed in R using
287 Seurat v5.1.0 and CellChat version 2.1.2. Graphs were generated in GraphPad Prism, the R
288 packages Seurat v5.1.0[36], ggplot2 version 3.5.1, scCustomize version 3.0.1, and Nebulosa
289 version 1.14.0[31] in R version 4.4.0, QuPath, or Omiq.ai. Differences were determined between
290 two groups by Mann-Whitney test or between greater than two groups by analysis of variance
291 (ANOVA) followed by Tukey post-hoc test.

292 **Results**

293 **Adaptive and innate immune cells are enriched in the fibrotic niche of human MASH**

294 To investigate immune cell proportions in human fibrotic MASH livers, a bulk RNA-seq dataset
295 consisting of over 200 NAFLD, now referred to as metabolic dysfunction-associated steatotic liver
296 disease (MASLD), patient biopsies[37] (GSE135251) was deconvoluted to predict liver non-
297 parenchymal cell (NPC) fraction frequencies from patients stratified by fibrosis stage (F0-F2 vs
298 F3-F4) (Figure 1A). This analysis revealed a significant increase in the predicted frequency of
299 CD8 T cells in patients with high Non-Alcoholic Steatohepatitis Activity Score (NAS; 6-8) or severe
300 fibrosis (F3-F4) (Figure 1B). Immunofluorescence (IF) of human liver sections delineated α-SMA$^+$
301 scar regions, which were enriched for CD3$^+$, CD8$^+$, and MHC-II$^+$ cells in patients with severe (F3-
302 F4) compared to minimal (F1-F2) fibrosis (Figure 1C). Cyclic immunofluorescence (cycIF) was
303 performed to quantify frequencies of CD3$^+$CD8$^+$ T cells and MHC-II$^+$ myeloid cells within liver scar
304 regions (Figure 1D-F). Increased CD3$^+$CD8$^+$ T cell percentages were significantly associated with
305 higher NAS (driven by lobular inflammation and ballooning) and fibrosis (Figure 1E,F),
306 corroborating the bulk deconvolution results (Figure 1B). Conversely, MHC-II$^+$ cell enrichment was
307 specific to fibrosis severity and did not vary with other NAS parameters (Figure 1E,F). Collectively,
308 these data establish that both adaptive and innate immune cells are spatially localized to the
309 fibrotic niche in human MASH livers, though they associate with distinct disease hallmarks.

310

311 **Auto-aggressive CD8 T cells accumulate in human fibrotic MASH and are associated with**
312 **disease severity**

313 Bulk RNA-seq datasets (GSE135251) were used to build on the established model of auto-
314 aggressive CXCR6$^+$ CD8 T cell-mediated, FASLG-dependent hepatocyte death in MASH[21]. *FAS*
315 gene expression was significantly increased in patients with high NAS or advanced fibrosis
316 (Figure 2A), while *FASLG*, which is expressed by NK cells and ILC1s in addition to T cells, neither
317 correlated with NAS nor fibrosis (Figure 2B). Deconvoluted CD8 T cells, as characterized in Figure

318 1A, were then scored with an auto-aggressive CD8 T cell signature, as previously described[21].
319 CD8 T cells from patients with high NAS or advanced fibrosis were enriched for the auto-
320 aggressive CD8 T cell signature (Figure 2C). Robust FASLG protein expression was confirmed
321 by IF in fibrotic regions, co-localizing with $CD3^+$ and $CD8^+$ immune cells (Figure 2D,E). FASLG
322 intensity was highest within CD8 T cells (Figure 2E), with the abundance of $FASLG^+$ CD8 T cells
323 increased in livers from patients with high NAS (driven by lobular inflammation) or those with
324 advanced fibrosis (Figure 2F,G). These data suggest that auto-aggressive, FASLG-expressing
325 CD8 T cells accumulate in the fibrotic niche in human MASH and may contribute to progressive
326 liver injury.
327
328 **CD8 T cells preferentially accumulate in preclinical models of fibrosing MASH**
329 The presence of T cells was further characterized across preclinical MASH and fibrosis models
330 induced in *C57BL/6* wild-type (WT) mice at 6 weeks of age by chemical compounds (*i.e.,* CCl_4)
331 and/or dietary regimens (*i.e.,* choline-deficient (CDA) or HFD consisting of 40% fat, 20% fructose,
332 2% cholesterol). Fibrosis was present in all mice, as assessed by picro Sirius Red staining and
333 imaged by either brightfield or polarized light, the latter providing improved and specific
334 visualization of intercellular fibrosis (Figure 3A). Lymphocytes, identified by CD3 IHC staining,
335 accumulated around the “crown like” structures of fatty hepatocytes (Figure 3B), consistent with
336 the reported auto-aggressive T cell function of killing lipid-laden hepatocytes in proximity[21]. The
337 proportion of CD8 T cells was significantly increased only in MASH livers with significant steatosis,
338 such as CDA and HFD, but not CCl_4 alone (Figure 3C). Thus, the 40-week HFD model, mimicking
339 MASH with fibrosis and enrichment of CD8 T cells, was selected as the optimal model for this
340 study[38]. Single-cell RNA-seq (scRNA-seq) profiling of chow and HFD livers at 40 weeks revealed
341 a diverse immune landscape (Figure 3D, Supplementary Figure 1A,B). Livers of HFD-fed mice
342 exhibited marked increases in the frequencies of CD8 T cells and myeloid cells (*i.e.,*

343 monocytes/macrophages, dendritic cells), reflecting an exacerbated inflammatory state (Figure
344 3E), similar to human disease.
345
346 **CD8 T cells display distinct transcriptional and phenotypic features linked with auto-**
347 **aggression and activation in livers of chronic HFD-fed mice**
348 To further characterize adaptive inflammation in HFD-fed mice, lymphocytes from scRNA-seq
349 were subclustered and annotated (Figure 4A, Supplementary Figure 2A). Remodeling of the
350 lymphocyte landscape in livers of HFD-fed mice was evident by the increase of mature CD8 T cell
351 subsets and reduction of naive and tissue-resident populations compared to chow-fed mice
352 (Figure 4B). Auto-aggressive CD8 T cells were delineated using joint density approximation
353 defined by a signature of key functional markers previously described (*Cxcr6*, *Il2rb*, *Pdcd1*, *Fasl*,
354 *Cd3e*)[21] (Figure 4C). To complement these transcriptomic observations, protein expression on
355 CD8 T cells was profiled by UMAP dimensionality reduction and unbiased clustering of flow
356 cytometry data (Figure 4D, E). Ten phenotypically distinct CD8 T clusters were identified (C1-C10)
357 (Figure 4D), with clusters C1, C6-C10 predominantly enriched in livers of HFD-fed mice (Figure
358 4D, E). Cluster C1 presented high expression of auto-aggressive and exhaustive CD8 T cell
359 markers, including FASLG and PD1, respectively (Figure 4F). Chronic HFD increased the
360 frequency of $CD44^{+}FASLG^{+}CXCR6^{hi}$ CD8 T cells, reduced homeostatic tissue-resident
361 macrophage- (TRM)-like cells ($CD69^{+}PD1^{+}$), and drove effector populations toward an exhausted
362 phenotype ($CD69^{-}PD1^{+}$) (Figure 4G-J).
363
364 **Livers of HFD-fed *Tcrb*-deficient mice show persistent cell death and scarring with rebound**
365 **γδ T cell accumulation**
366 To assess the therapeutic potential of autoimmunity disruption in chronic diet-induced liver injury
367 and fibrosis, *Tcrb*-deficient mice (*Tcrb*-/-), which lack conventional TCRαβ T cells, were challenged
368 with the 40-week HFD. All HFD-fed mice exhibited progressive weight gain, with *Tcrb*-deficient

369 mice showing a modest but significant reduction in body weight increase compared to WT
370 counterparts (Figure 5A,B). Liver index was comparable between genotypes and remained
371 markedly elevated relative to chow-fed baseline (dotted line, Figure 5C). Serum transaminases
372 (*i.e.,* ALT and AST) were lower in HFD-fed *Tcrb*-deficient compared to WT mice (~450 and ~600
373 ALT U/L, respectively), but remained higher than chow-fed baseline levels (~50 ALT U/L),
374 indicating persistent hepatocellular injury (Figure 5D,E). Histological assessment revealed
375 extensive steatosis and collagen deposition in both WT and *Tcrb*-deficient mice fed HFD, with no
376 significant difference in fibrosis (Figure 5F,I). Although liver injury was reduced, cell death
377 assessed by TUNEL^{+} staining was increased in *Tcrb*-deficient mice (Figure 5G,J), while cleaved
378 Caspase-3 showed no significant change (Figure 5H,K), contrasting with previous reports in mice
379 lacking both conventional αβ and γδ T cells (*Tcrb/d*-/-)[21]. As expected, *Tcrb*-deficient mice lacked
380 conventional CD8 T cells; however, this was accompanied by a significant rebound or
381 compensatory accumulation of intrahepatic γδ T cells (Figure 5L). These data demonstrate that
382 the loss of TCRαβ cells did not mitigate chronic HFD-induced cell death or fibrosis, but rather
383 promoted alternative and potentially compensatory T cell responses.
384
385 **HFD-fed *Tcrb*-deficient mice present exacerbated hepatic pro-fibrotic type 3 inflammation**
386 Liver samples from *Tcrb*-deficient mice fed control chow or HFD were also profiled by scRNA-seq
387 (Supplementary Figure 3A-D) and intrahepatic lymphocytes were subclustered, revealing a
388 diverse γδ T cell compartment (Figure 6A, Supplementary Figure 3E). Notably, application of the
389 functional auto-aggressive signature (*Cxcr6*, *Il2rb*, *Pdcd1*, *Fasl*, *Cd3e*) identified a population of
390 γδ T cells with transcriptional similarity (Figure 6B). Furthermore, a cluster with co-localized
391 expression of type 3 cytokines, namely *Il17a* and *Tnf,* was highly prevalent during chronic HFD
392 (Figure 6A-C). Intrahepatic leukocytes (IHLs) were then isolated and restimulated from WT and
393 *Tcrb*-deficient livers for functional assessment of cytokine output (Figure 6D). Compared to WT,
394 HFD-fed *Tcrb*-deficient mice released increased levels of type 1 pro-inflammatory (IL6, TNFα) and

395 type 3 pro-fibrotic (IL17A, GMCSF) factors, alongside T cell-inducing cytokines (IL-12p40, IL-
396 12p70, IL-23a), but not type 2 cytokines (IL-5) (Figure 6D,E). Particularly, IL6, IL-17A and TNFα
397 were significantly elevated in IHLs from HFD-fed *Tcrb*-deficient mice (~550, ~1000 and ~600
398 pg/mL, respectively) when compared to their WT counterparts (~175, ~600 and ~100 pg/mL,
399 respectively) (Figure 6E). These findings suggest that the absence of conventional CD8 T cells
400 promotes compensatory γδ T cell expansion in the liver and a pro-fibrotic cytokine milieu
401 dominated by IL-17A and TNFα, which may synergize to drive hepatotoxicity and fibrotic
402 remodeling.
403
404 **Pro-fibrotic SPP1$^+$ scar-associated macrophages (SAMs) persist in MASH livers in the**
405 **absence of conventional αβ T cells**
406 Given that *Tcrb*-deficiency failed to prevent HFD-induced fibrosis in mice, myeloid subsets were
407 subsequently investigated. Livers of HFD-fed mice analyzed by scRNA-seq revealed an increase
408 in myeloid diversity in HFD-fed animals compared to chow-fed controls of both WT and *Tcrb*-
409 deficient mice (Figure 7A-F, Supplementary Figure 4A,B). In both genotypes, HFD increased the
410 abundance of SPP1$^+$ SAMs, defined by the expression of the Fab5 signature (*Cd9*, *Trem2*, *Cd63*,
411 *Fabp5*, *Gpnmb*, *Spp1*)[23] (Figure 7B,E). The presence of SPP1$^+$ SAMs was assessed at the protein
412 level by flow cytometry, where HFD led to the specific accumulation of CD9$^+$TREM2$^+$Galectin-
413 3$^+$GPNMB$^+$ cells within F4/80$^+$Ly6C^{lo} macrophages, in both WT and *Tcrb*-deficient mice (Figure
414 7G). While the relative abundance of myeloid cells was consistent across conditions, HFD led to
415 a significant increase in CD9$^+$TREM2$^+$Galectin-3$^+$GPNMB$^+$ macrophages compared to normal
416 chow, irrespective of genotype (Figure 7H). Heatmap profiling of flow cytometry-based protein
417 expression further showed the upregulation of SAM-specific markers in fibrotic livers of HFD-fed
418 mice, with comparable expression patterns between WT and *Tcrb*-deficient mice (Figure 7I).
419 Finally, cycIF of WT and *Tcrb*-deficient HFD livers showed a fibrotic niche architecture
420 characterized by the accumulation of GMCSF$^+$IL17A$^+$MMP9$^+$ neutrophils, SPP1$^+$GPNMB$^+$FABP5$^+$

421 SAMs[23], and RBPJ$^+$ macrophages[39] in proximity of Desmin$^+$ myofibroblasts forming crown-like
422 structures (Figure 7J). Thus, HFD-induced SPP1$^+$ SAM expansion in liver disease occurs
423 independently of conventional αβ T cells, implicating macrophage-driven mechanisms in fibrosis
424 persistence.
425
426 **CXCL16 positive myeloid cells retain CD8 T cells in fibrotic niches of human and mouse**
427 **liver**
428 Transcriptomic cell-cell interaction analysis predicted a significant increase in the number of
429 ligand-receptor communications between T cells and myeloid cells in livers of both WT and *Tcrb*-
430 deficient HFD-fed mice compared to chow-fed controls (Figure 8A). Interactions were filtered to
431 chemokine/receptor pairs upregulated in HFD and revealed CXCL16 and CXCR6 as a preserved
432 chemotactic axis between myeloid cells and both αβ and γδ T cells within fibrotic liver tissue
433 (Figure 8B). These findings were confirmed using human liver tissue from MASH patients with
434 either early-stage disease (F0-F2) or advanced fibrosis (F3-F4). Increased CXCL16$^+$ and
435 GPNMB$^+$ macrophages were observed by IF in α-SMA$^+$ fibrotic regions (Figure 8C). CycIF
436 analysis confirmed CXCL16$^+$ localization in scar regions co-populated by CD8 T cells and SPP1$^+$
437 SAMs (Figure 8D). Spearman correlation between the frequencies of cells identified by cycIF and
438 components of NAS and fibrosis revealed a positive correlation between CXCL16$^+$ cells and the
439 accumulation of both total and FASLG$^+$ CD8 T cells in human MASH livers (Figure 8E,F).
440 Moreover, the frequency of SPP1$^+$GPNMB$^+$FABP5$^+$ SAMs correlated specifically with fibrosis,
441 over other histological features (NAS and steatosis), supporting their pro-fibrotic nature (Figure
442 8G,H). These findings identify CXCL16-CXCR6 signaling as a key mechanism by which SAMs
443 and other myeloid cells orchestrate immune cell positioning, recruiting T cells within the fibrotic
444 microenvironment. Myeloid cells, particularly through SAM expansion, contribute to bystander
445 CD8 and γδ T cell accumulation in MASH and are thus sufficient for liver fibrosis.

446 **Discussion**

447 The immunopathological landscape of MASH has often featured the accumulation of T cells, due
448 to the metabolic syndrome, dysbiosis and hepatocellular cell death triggering chemotactic
449 responses to the liver[4]. T cells contribute to fibrosis progression via either pro-inflammatory and
450 pro-fibrotic cytokine secretion or cytotoxic pathways. We and others reported the dysregulation of
451 the T effector (Th2/Th17) to T regulatory cell ratio in MASH, contributing to the pro-fibrotic type 2
452 and 3 mixed inflammatory milieu[11,18]. MASH livers also feature a lipotoxic environment that affects
453 survival of CD4 T cells and leads to a significant accumulation of CD8 T cells[19]. Here, we
454 confirmed first by deconvolution of a bulk RNA-seq dataset of over 200 patients (Figure 1A,B)
455 and in an independent cohort of FFPE MASH livers using cycIF (Figure 1C-E) that CD8 T cell
456 accumulation in the liver correlates with NAS, lobular inflammation and fibrosis stage. CD8 T cells
457 may expand in livers due to the presence of $XCR1^+$ cDC1s, and chronic antigenic stimulation,
458 promoting inflammation and hepatocellular damage[20,40]. Liver homing/resident $CXCR6^+$ CD8 T
459 cells, rendered auto-aggressive through IL-15-driven transcriptional reprogramming and
460 metabolic activation, were reported to contribute to FASLG-mediated hepatocyte apoptosis in
461 preclinical models of MASH[21]. This auto-aggressive signature was significantly enriched in livers
462 with high NAS (6-8) and fibrosis (F3-4), as demonstrated by deconvoluted bulk RNA-seq (Figure
463 2C). Using cycIF, we confirmed that auto-aggressive CD8 T cells (defined by the co-expression
464 of FASLG, CD3 and CD8) correlated with lobular inflammation and were enriched in fibrotic scars
465 (Figure 2D-G) in human MASH livers.

466

467 In line with previous reports, CD3 T cells were located in areas of fibrosis in both toxin- and diet-
468 induced fibrosis models (Figure 3A, B). However, the frequency of CD8 T cells was significantly
469 increased only in models with severe and chronic steatohepatitis such as CDA and HFD. This
470 could explain the previous observation that adaptive immune cells may not contribute to fibrosis
471 in toxin-dependent preclinical models. Indeed, expansion of CD8 T cells in MASH appears to be

472 clonal[40], as a result of lipid accumulation in the liver and potential dysbiosis. Additionally, scRNA-
473 seq and flow cytometry confirmed that chronic western-diet (high fat, fructose and cholesterol)
474 induced an auto-aggressive CD8 T cell phenotype ($CD44^{hi}CXCR6^{+}FASLG^{+}PD1^{+}$), as previously
475 reported using CDHFD[21]. Genetic ablation of conventional αβ T cells using *Tcrb*-deficient mice
476 led to a modest improvement of certain physiopathological features of MASH, such as percent
477 body weight and serum ALT (Figure 5A-D). However, serum ALT remained nearly ten times higher
478 than mice on chow diet, which was consistent with the lack of improvement in cell death, assessed
479 by $TUNEL^{+}$ and cleaved-Caspase-3^{+} cell counts, in livers of HFD-fed *Tcrb*-deficient mice (Figure
480 5G,H,J,K). Foreseeably, this was associated with no significant improvement in fibrosis, as
481 determined by both picro Sirius Red staining and hydroxyproline quantification (Figure 5F,I).
482 These results contrast with the recent observation linking both CD4 and CD8 T cells to the
483 amplification of inflammation and fibrosis in MASH[41].
484
485 The contribution of γδ T cells in the liver has been linked to both fibrosis progression and
486 resolution, depending on their phenotype. These γδ T cells can limit hepatocellular death via the
487 secretion of IL-22, activation of hepatic stellate cells (HSCs) via the secretion of IFNγ, and mediate
488 clearance of activated HSCs via FAS/FASLG[42]. The role of auto-aggressive CD8 T cells in MASH
489 was initially defined in mice lacking both αβ and γδ T cells (*Tcrb/d*-double-deficient)[21]. In our case,
490 a significant compensatory rebound in γδ T cells in livers of *Tcrb*-deficient mice was observed
491 after chronic HFD (Figure 5L). The γδ T cells in HFD-fed *Tcrb-/-* mice displayed a diverse array of
492 pro-fibrotic phenotypes, including a cell cluster enriched for the functional auto-aggressive
493 signature (*Cxcr6*, *Il2rb*, *Pdcd1*, *Fasl*, *Cd3e*), originally described in CD8 T cells. Another cluster of
494 γδ T cells showed co-expression of *Il17a* and *Tnf,* consistent with the significantly higher level of
495 IL-17A, GMCSF and TNFα in re-stimulated IHLs from *Tcrb*-deficient mice when compared to WT
496 mice following 40 weeks of chronic HFD (Figure 6D,E). Notably, IL-17A is a pro-inflammatory and
497 pro-fibrotic cytokine associated to fibrosis progression in many types of liver injury and tissues.

498 IL-17A facilitates TNF-driven hepatotoxicity in steatotic hepatocytes, amplifying Caspase-2-
499 SREBP1/2-mediated lipogenesis and inflammation[43,44]. IL-17A also sensitizes HSCs to the action
500 of TGFβ via stabilization of the TGF-β-RII on the surface. Altogether, our results indicate that γδ
501 T cells expand in the absence of conventional αβ T cells and maintain a milieu favorable, skewed
502 towards type 3 inflammation, to the development of the fibrotic niche[45].
503
504 Fibrotic scars of both WT and *Tcrb*-deficient mice showed myeloid cell dysregulation, particularly
505 characterized by the loss of tissue-resident Kupffer cells and accumulation of SPP1$^+$ SAMs with
506 a Fab5 signature[23]. Lack of conventional αβ T cells neither impacted the overall frequency,
507 transcriptomic signature nor phenotype of SPP1$^+$ SAMs (Figure 7A-I). Histologically, scars from
508 WT and *Tcrb*-deficient mice showed similar accumulation of IL17A$^+$GMCSF$^+$MMP9$^+$ neutrophils
509 in proximity of myofibroblasts and SPP1$^+$GPNMB$^+$FABP5$^+$ macrophages. SPP1$^+$ SAMs are
510 associated with fibrosis progression across tissues, degrade normal extracellular matrix (ECM;
511 Collagen IV) and increase deposition of pathogenic ECM (Collagen I)[23]. Accordingly, these cells
512 accumulated in human MASH livers with severe fibrosis at the scar border and correlated with
513 histopathological fibrosis grade (Figure 8C,D,H). Unlike CD8 T cells, SPP1$^+$ SAMs neither
514 correlated with increased NAS, lobular inflammation, hepatocyte ballooning nor steatosis (Figure
515 8G), reinforcing their pro-fibrotic association. Moreover, we found increased protein expression of
516 RBPJ (Figure 7J), a transcription factor involved in pathogenic monocyte to macrophage (MDM)
517 differentiation, in myeloid cells associated with fibrosis in livers from HFD-fed mice[39].
518
519 Finally, we investigated whether myeloid cells in the liver fibrotic niche may contribute to the
520 accumulation of CXCR6$^+$ T cells during MASH. Unbiased chemokine/receptor interaction
521 predictions identified a conserved mechanism of myeloid-driven T cell recruitment to the fibrotic
522 niche in livers of both *Tcrb*-deficient and WT HFD-fed mice (Figure 8A,B). These data show that
523 macrophages/monocytes and dendritic cells are sources of CXCL16 that bind CXCR6 on auto-

524 aggressive CD8 T cells and γδ T cells. Taken together, these results indicate that myeloid cells,
525 rather than conventional adaptive immune cells, are pivotal regulators of inflammation at the
526 fibrotic niche. While broad neutralization of myeloid cells via inhibition of CCR2 showed limited
527 efficacy in patients, due to its broad effect, it is possible that more refined myeloid cell inhibition
528 would be beneficial[46-50]. Preventing monocyte recruitment by CCR2 antagonism not only limits
529 the development of pathogenic MDMs, but also the ability of monocytes to restore the pool of
530 depleted tissue resident macrophages (*i.e.,* Kupffer cells) in MASH. As an alternative therapeutic
531 approach, myeloid cell inhibition of RBPJ blunted differentiation towards $SPP1^+$ SAMs, improved
532 recovery of Kupffer cells and induced patrolling monocytes, reducing inflammation and fibrosis in
533 preclinical MASH models[39].
534
535 This study contextualizes the roles of adaptive and innate immunity within a broader
536 immunological landscape of the fibrotic niche. Since our data indicate redundancy between
537 $CXCR6^+$ lymphocytes in MASH, we suggest that targeting the myeloid cells responsible for
538 CXCL16 production and HSC activation in combination with anti-steatotics will yield superior anti-
539 fibrotic activity. In conclusion, our study demonstrates that myeloid cells are master regulators of
540 fibrosis and fibrosis-associated adaptive immunity, redefining the immune-mediated fibrotic niche
541 in MASH.

542 **Figures and figure legends**

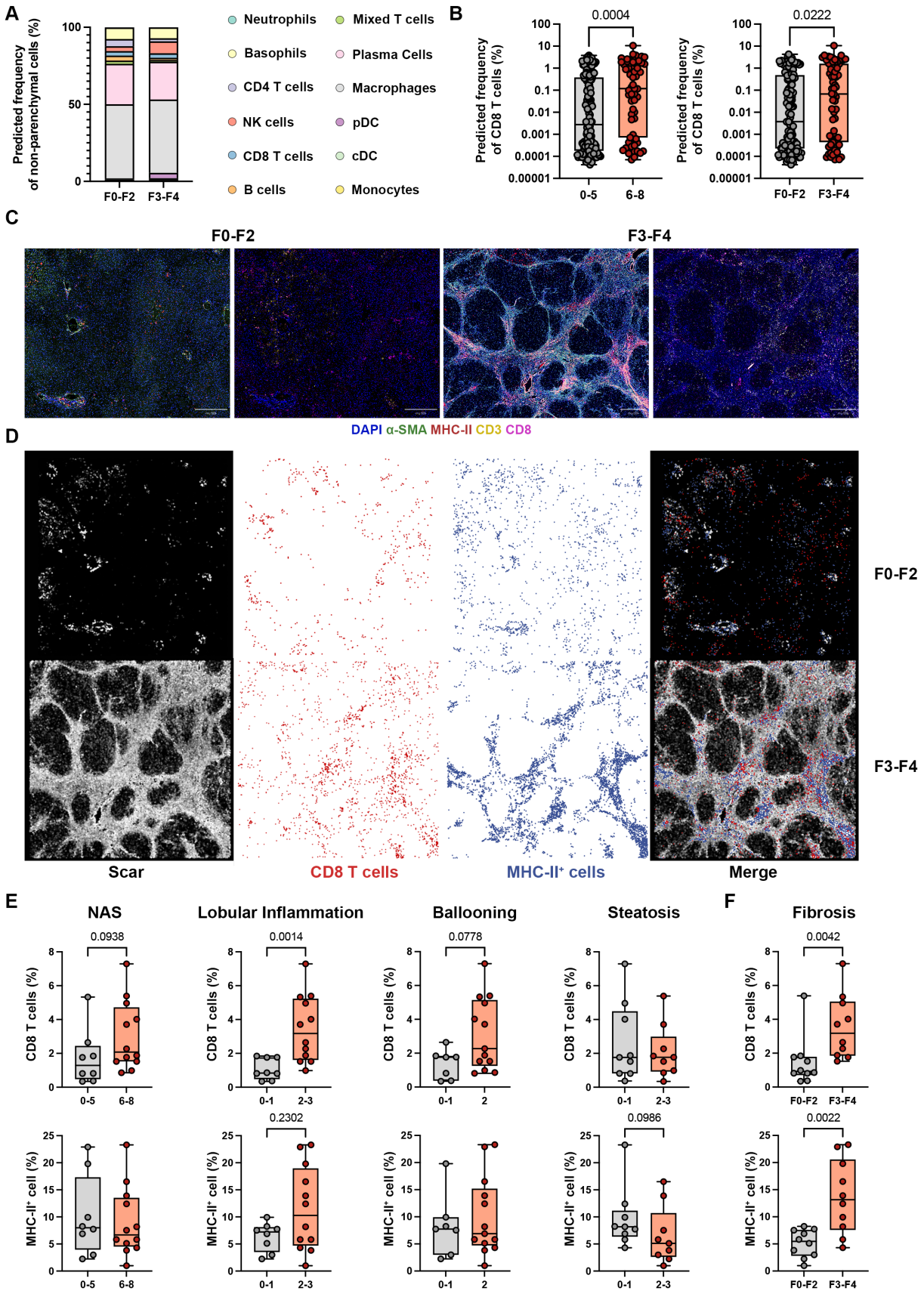
A
Predicted frequency of non-parenchymal cells (%)
F0-F2
F3-F4
Neutrophils
Basophils
CD4 T cells
NK cells
CD8 T cells
B cells
Mixed T cells
Plasma Cells
Macrophages
pDC
cDC
Monocytes
B
Predicted frequency of CD8 T cells (%)
0.0004
0-5
6-8
0.0222
F0-F2
F3-F4
C
F0-F2
F3-F4
DAPI α-SMA MHC-II CD3 CD8
D
F0-F2
F3-F4
Scar
CD8 T cells
MHC-II⁺ cells
Merge
E
NAS
Lobular Inflammation
Ballooning
Steatosis
F
Fibrosis
CD8 T cells (%)
MHC-II⁺ cell (%)
0.0938
0.0014
0.0778
0.0042
0.2302
0.0986
0.0022
0-1
2-3
2

543

544 **Figure 1: Accumulation of CD8 T cells and myeloid cells in scar in human MASH.**

545 (A) Predicted frequency from deconvoluted bulk RNA-seq (GSE135251) of immune-cells within
546 the non-parenchymal fraction between F0-F2 and F3-F4 patients. (B) Box plot showing increased
547 predicted frequency of CD8 T cells in NAS 6-8 and F3-F4 patients. (C) Representative
548 immunofluorescence of α-SMA (green), MHC-II (red), CD3 (yellow) and CD8 (magenta) from F0-
549 F2 and F3-F4 patient liver sections. (D) cycIF representative images of liver sections showing
550 scar (α-SMA$^+$ cells, grey), CD3$^+$CD8$^+$ T cells (red), MHC-II$^+$ cells (blue) and merge overlay from
551 patients with minimal fibrosis (F0-F2) or severe fibrosis (F3-F4). (E-F) Box plots showing CD8$^+$ T
552 cells (top) and MHC-II$^+$ (bottom) cell frequencies from cycIF according to NAS, lobular
553 inflammation, ballooning, steatosis (E) and fibrosis (F) from 20 patients with MASH. Data are
554 presented as min – max values and median box plots. Box plot statistical analysis was performed
555 by Mann-Whitney test.

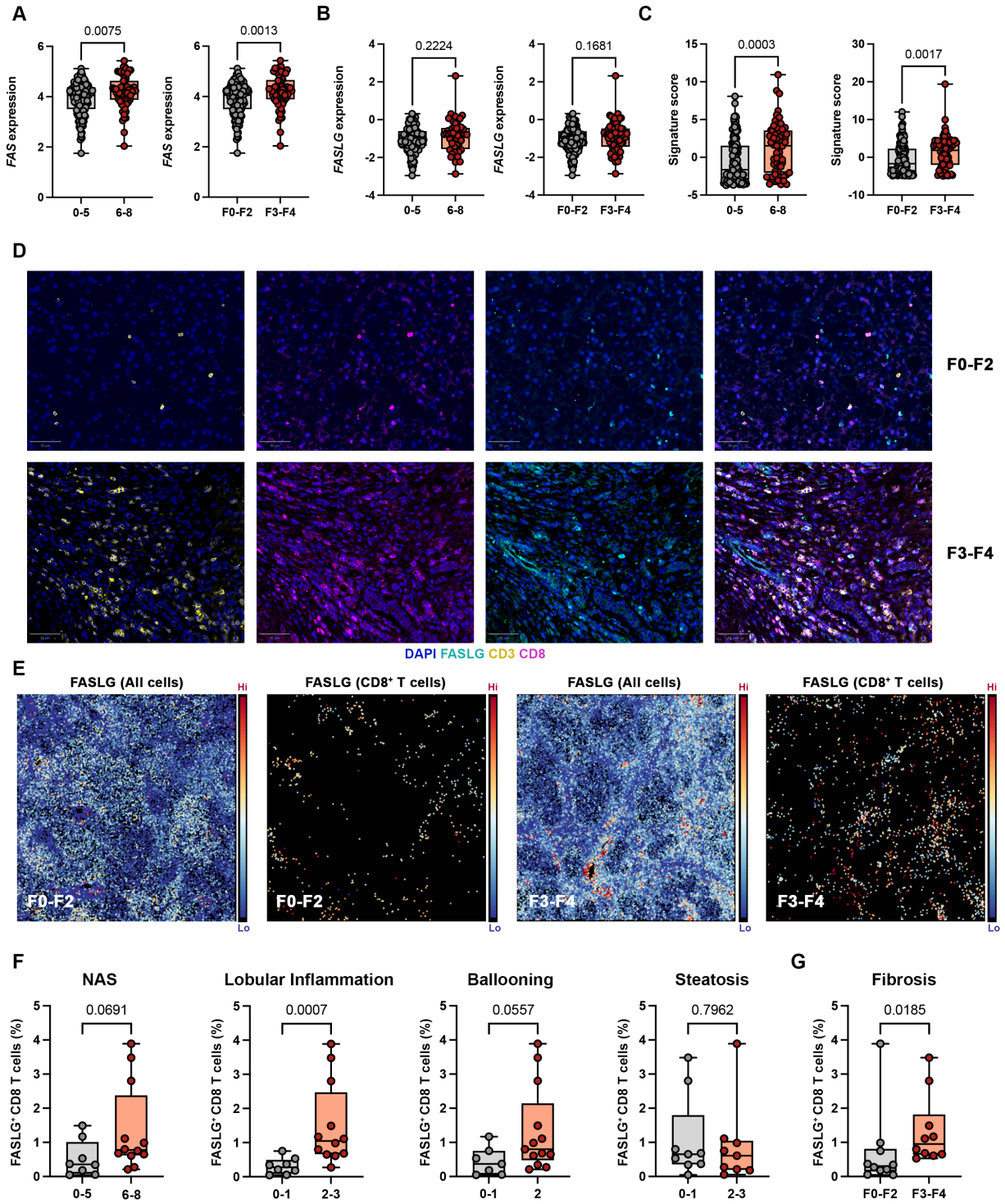
A
0.0075
FAS expression
0-5
6-8
0.0013
FAS expression
F0-F2
F3-F4
B
0.2224
FASLG expression
0-5
6-8
0.1681
FASLG expression
F0-F2
F3-F4
C
0.0003
Signature score
0-5
6-8
0.0017
Signature score
F0-F2
F3-F4
D
F0-F2
F3-F4
DAPI FASLG CD3 CD8
E
FASLG (All cells)
FASLG (CD8⁺ T cells)
FASLG (All cells)
FASLG (CD8⁺ T cells)
Hi
Lo
F0-F2
F0-F2
F3-F4
F3-F4
F
NAS
0.0691
Lobular Inflammation
0.0007
Ballooning
0.0557
Steatosis
0.7962
G
Fibrosis
0.0185
FASLG⁺ CD8 T cells (%)
0-5
6-8
0-1
2-3
0-1
2
0-1
2-3
F0-F2
F3-F4

556

557

558 **Figure 2: Accumulation of auto-aggressive FASLG$^+$ CD8 T cells in scar in human MASH.**
559 (A-C) Bulk RNA-seq expression of *FAS* (A, global expression), *FASLG* (B, global expression) and
560 auto-aggressive signature score (C, in deconvoluted CD8 T cells) based on fibrosis score (F0-F2,
561 grey vs F3-F4, red). (D) Representative IF images of CD3 (yellow), CD8 (magenta) and FASLG
562 (cyan) from F0-F2 and F3-F4 MASH livers. (E) cycIF representative images showing expression
563 intensity (blue=low and red=high) of FASLG in all cells vs CD8 T cells from F0-F2 and F3-F4
564 MASH livers. (F-G) Box plots showing the frequency of FASLG$^+$ CD8 T cells with NAS, lobular
565 inflammation, ballooning, steatosis (F) and fibrosis (G). Data are presented as min – max values
566 and median box plots. Box plot statistical analysis was performed by Mann-Whitney test.

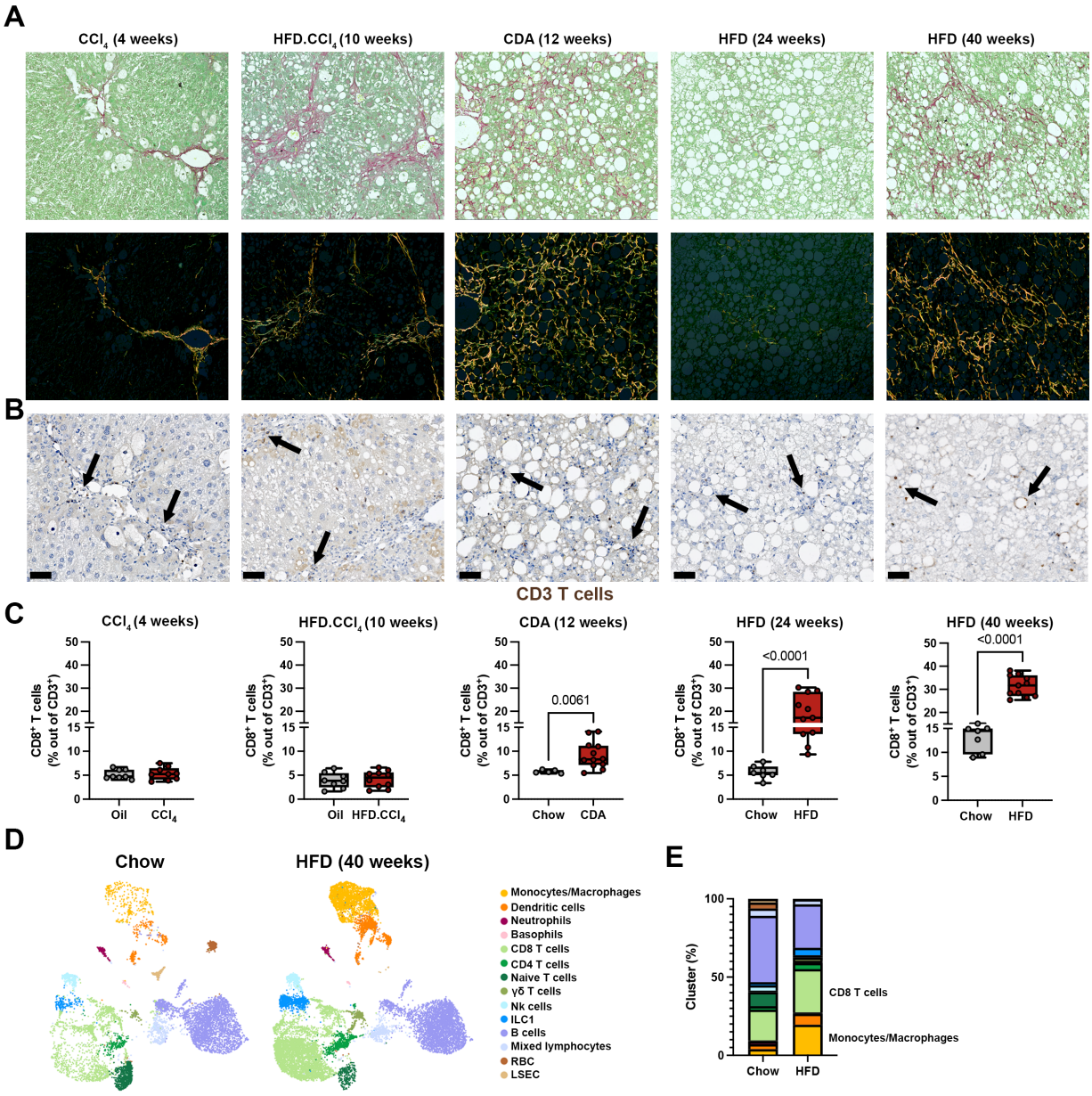
A
CCl4 (4 weeks)
HFD.CCl4 (10 weeks)
CDA (12 weeks)
HFD (24 weeks)
HFD (40 weeks)
B
CD3 T cells
C
CCl4 (4 weeks)
HFD.CCl4 (10 weeks)
CDA (12 weeks)
HFD (24 weeks)
HFD (40 weeks)
CD8+ T cells (% out of CD3+)
Oil
CCl4
HFD.CCl4
0.0061
<0.0001
<0.0001
Chow
CDA
HFD
D
Chow
HFD (40 weeks)
Monocytes/Macrophages
Dendritic cells
Neutrophils
Basophils
CD8 T cells
CD4 T cells
Naive T cells
γδ T cells
Nk cells
ILC1
B cells
Mixed lymphocytes
RBC
LSEC
E
Cluster (%)
CD8 T cells
Monocytes/Macrophages
Chow
HFD

567

568

569 **Figure 3. Chronic high-fat diet (HFD) leads to increased frequency of CD8 T cells in**
570 **preclinical MASH models.**
571 (A) Representative brightfield (top) and polarized light (bottom) picro Sirius Red images from 4
572 weeks of CCl_4, 10 weeks of HFD/CCl_4 ,12 weeks of CDA, or 24 and 40 weeks of HFD, respectively.
573 (B) Representative immunohistochemistry images of CD3 T cells in hepatic fibrotic regions of
574 mice challenged with CCl_4, HFD/CCl_4, CDA, 24 or 40 weeks HFD, respectively. (C) Box plots
575 showing the frequency of intrahepatic CD8 T cells from mice challenged with CCl_4, HFD/CCl_4,
576 CDA, 24- or 40 weeks HFD measured by flow cytometry, respectively. (D) UMAP visualization of
577 immune cells from scRNA-seq from chow (left) and HFD (right) livers at 40 weeks post study start
578 (n=3 mice per group). (E) Stacked bar chart showing the relative frequency of immune cells from
579 scRNA-seq. Data are presented as min – max values and median box plots. Box plot statistical
580 analysis was performed by Mann-Whitney test.

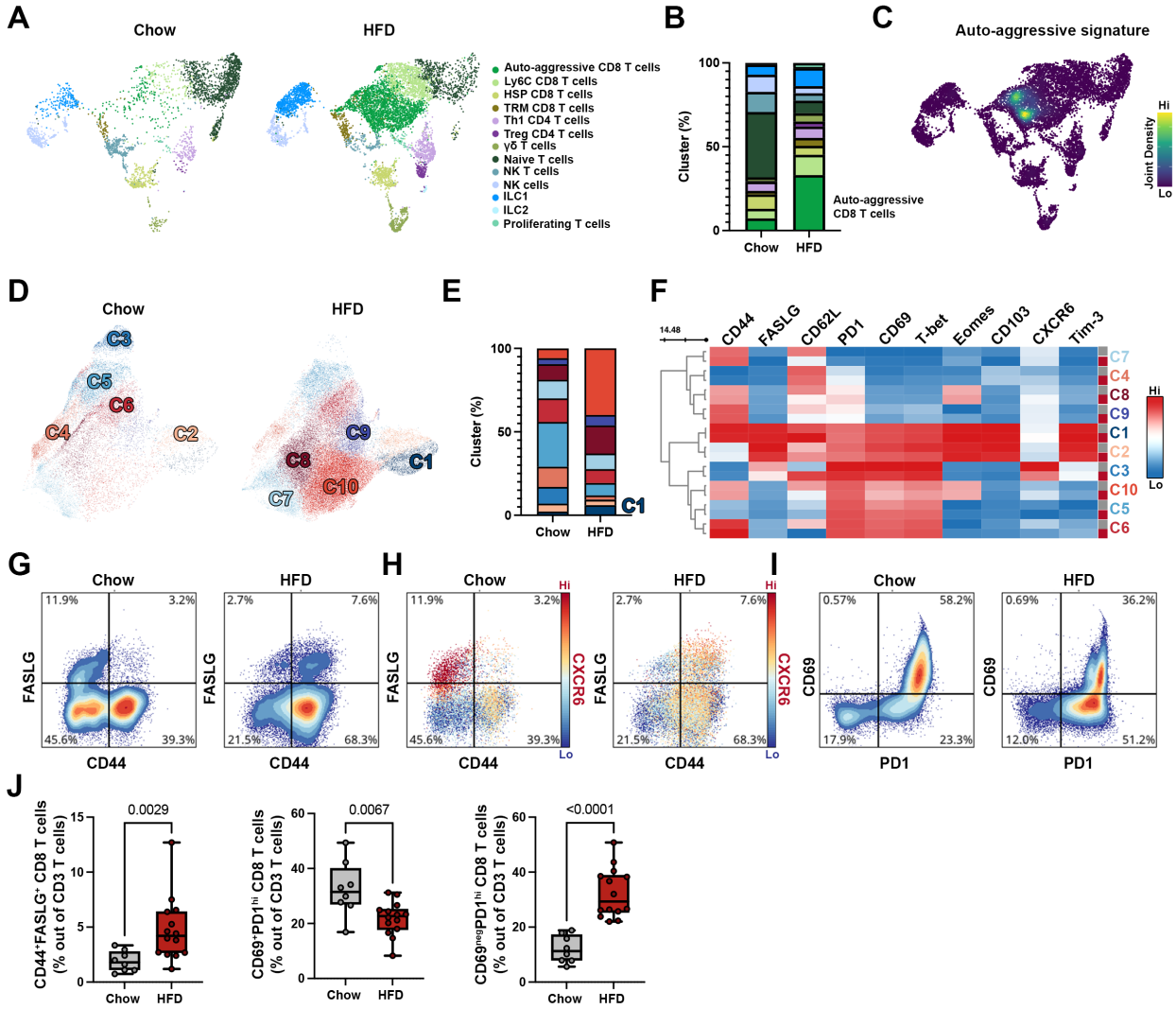
A
Chow
HFD
Auto-aggressive CD8 T cells
Ly6C CD8 T cells
HSP CD8 T cells
TRM CD8 T cells
Th1 CD4 T cells
Treg CD4 T cells
γδ T cells
Naive T cells
NK T cells
NK cells
ILC1
ILC2
Proliferating T cells
B
Cluster (%)
Auto-aggressive CD8 T cells
C
Auto-aggressive signature
Joint Density
Hi
Lo
D
C3
C5
C6
C4
C2
C9
C8
C1
C7
C10
E
Cluster (%)
F
14.48
CD44
FASLG
CD62L
PD1
CD69
T-bet
Eomes
CD103
CXCR6
Tim-3
C7
C4
C8
C9
C1
C2
C3
C10
C5
C6
G
FASLG
CD44
11.9%
3.2%
45.6%
39.3%
2.7%
7.6%
21.5%
68.3%
H
CXCR6
11.9%
3.2%
45.6%
39.3%
2.7%
7.6%
21.5%
68.3%
I
CD69
PD1
0.57%
58.2%
17.9%
23.3%
0.69%
36.2%
12.0%
51.2%
J
CD44+FASLG+ CD8 T cells (% out of CD3 T cells)
0.0029
CD69+PD1hi CD8 T cells (% out of CD3 T cells)
0.0067
CD69negPD1hi CD8 T cells (% out of CD3 T cells)
<0.0001
Chow
HFD

581

582

583 **Figure 4. Accumulation of FASLG^{+} auto-aggressive CD8 T cells in chronic HFD-fed mice.**
584 (A) UMAP visualization of lymphocytes from chow (left) and HFD (right) livers after 40 weeks. (B)
585 Stacked bar chart showing the frequency of different lymphocyte subsets from panel A and the
586 accumulation of auto-aggressive CD8 T cells (green) in HFD livers. (C) Joint density
587 approximation of the auto-aggressive signature (*Cxcr6*, *Il2rb*, *Pdcd1*, *Fasl*, *Cd3e*) enabling the
588 identification of FASLG^{+} auto-aggressive CD8 T cells. (D) UMAP visualization of 10 CD8 T cell
589 clusters identified by flow cytometry. (E) Stacked bar chart showing relative frequency of the 10
590 CD8 T cell clusters, shown as C1 to C10 from bottom to top, between chow and HFD livers. (F)
591 Clustered heatmap showing the relative log2FC change in the MFI of markers on the 10 CD8 T
592 cell clusters (grey=chow and red=HFD). (G-H) Representative FACS plots showing increased
593 frequency of CD44^{+}FASLG^{+} CD8 T cells (G), overlayed with CXCR6 MFI (H). (I) Representative
594 FACS plots showing the decreased frequency of tissue resident memory-like CD8 T cells
595 (CD69^{+}PD1^{+}) in HFD livers. (J) Box plots showing the relative frequency of
596 CD44^{+}FASLG^{+}CXCR6^{+} (auto-aggressive) CD8 T cells (left), CD69^{+}PD1^{hi} CD8 T cells (middle) and
597 CD69^{neg}PD1^{hi} CD8 T cells (right). Data are presented as min – max values and median box plots.
598 Box plot statistical analysis was performed by Mann-Whitney test.

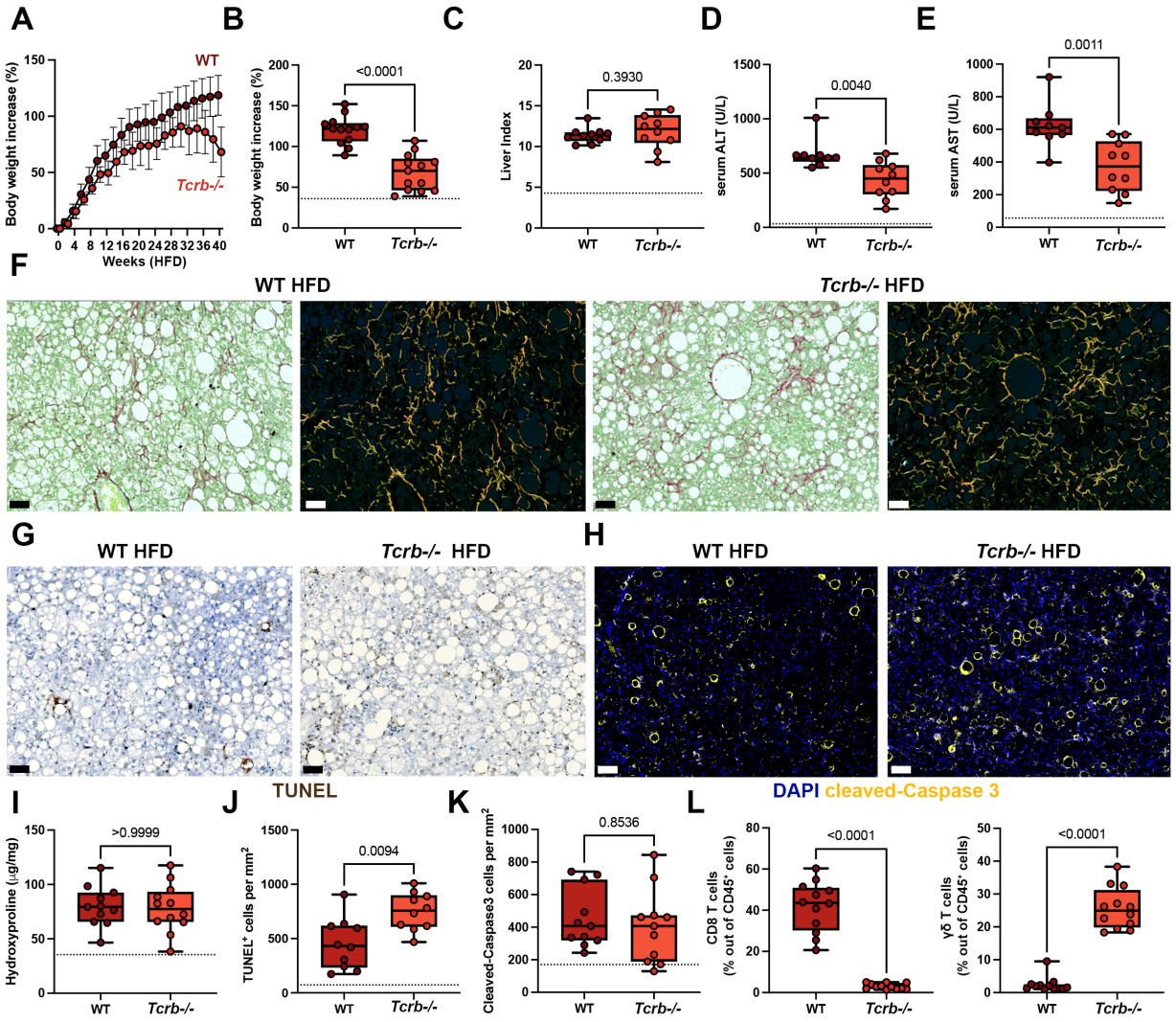
A
B
C
D
E
WT
Tcrb-/-
Body weight increase (%)
Weeks (HFD)
<0.0001
Body weight increase (%)
0.3930
Liver Index
0.0040
serum ALT (U/L)
0.0011
serum AST (U/L)
WT
Tcrb-/-
F
WT HFD
Tcrb-/- HFD
G
WT HFD
Tcrb-/- HFD
H
WT HFD
Tcrb-/- HFD
TUNEL
DAPI cleaved-Caspase 3
I
J
K
L
>0.9999
Hydroxyproline (µg/mg)
0.0094
TUNEL+ cells per mm2
0.8536
Cleaved-Caspase3 cells per mm2
<0.0001
CD8 T cells (% out of CD45+ cells)
<0.0001
γδ T cells (% out of CD45+ cells)

599

600 **Figure 5. *Tcrb* deficiency does not mitigates steatosis, epithelial/hepatocellular death or**
601 **fibrosis in chronic HFD-fed mice.**
602 (A-E) Body weight curves (A), percent increase in body weight after 40 weeks of HFD (B), liver
603 index (C), serum ALT (D) and serum AST (E) between WT (dark red) and *Tcrb-/-* (red) HFD-treated
604 mice. (F-H) Representative picro Sirius Red brightfield and polarized light (F), TUNEL staining (G)
605 and cleaved-Caspase 3 immunofluorescent (H) images from WT and *Tcrb-/-* HFD-treated mice.
606 (I-J) Box plots showing the quantification of hydroxyproline (I), $TUNEL^+$ cells per mm^2 (J) and
607 cleaved-Caspase 3^+ cells (K) between WT and *Tcrb-/-* HFD-treated mice. (L) Box plots showing
608 the relative frequency of conventional CD8 T cells and γδ T cells between WT and *Tcrb-/-* HFD-
609 treated mice. Data are presented as min – max values and median box plots. Box plot statistical
610 analysis was performed by Mann-Whitney test.

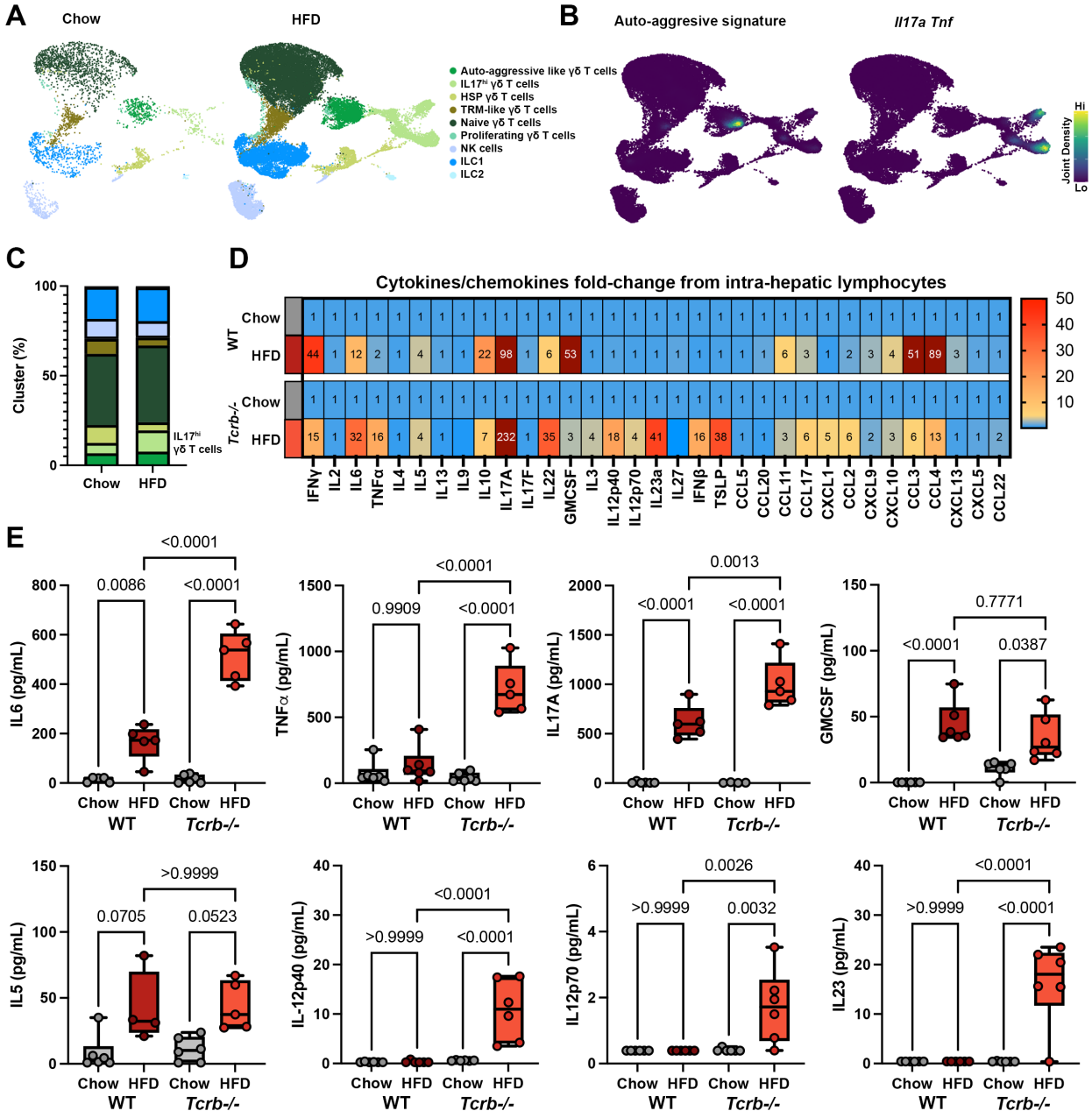
A
Chow
HFD
Auto-aggressive like γδ T cells
IL17hi γδ T cells
HSP γδ T cells
TRM-like γδ T cells
Naive γδ T cells
Proliferating γδ T cells
NK cells
ILC1
ILC2
B
Auto-aggresive signature
Il17a Tnf
Hi
Joint Density
Lo
C
Cluster (%)
IL17hi γδ T cells
Chow
HFD
D
Cytokines/chemokines fold-change from intra-hepatic lymphocytes
WT
Tcrb-/-
Chow
HFD
IFNγ IL2 IL6 TNFα IL4 IL5 IL13 IL9 IL10 IL17A IL17F IL22 GMCSF IL3 IL12p40 IL12p70 IL23a IL27 IFNβ TSLP CCL5 CCL20 CCL11 CCL17 CXCL1 CCL2 CXCL9 CXCL10 CCL3 CCL4 CXCL13 CXCL5 CCL22
E
IL6 (pg/mL)
TNFα (pg/mL)
IL17A (pg/mL)
GMCSF (pg/mL)
IL5 (pg/mL)
IL-12p40 (pg/mL)
IL12p70 (pg/mL)
IL23 (pg/mL)
Chow HFD Chow HFD
WT Tcrb-/-

611

612

613 **Figure 6. Loss of conventional CD8 T cells exacerbates pro-fibrotic type 3 inflammation.**
614 (A) UMAP visualization of lymphocytes from livers of *Tcrb-/-* mice on chow or HFD at 40 weeks
615 by scRNA-seq. (B) Joint density expression of the auto-aggressive signature (*Cxcr6*, *Il2rb*, *Pdcd1*,
616 *Fasl*, *Cd3e*) (left), *Il17a* and *Tnf* (right). (C) Stacked bar chart showing the frequency of
617 lymphocytes from *Tcrb-/-* mice on chow or HFD for 40 weeks. (D) Heatmap of cytokines, fold
618 change to chow (grey) mice, from re-stimulated IHLs isolated from WT (dark red) and *Tcrb-/-* (red)
619 HFD mice after 40 weeks. (E) Box plots showing the intrahepatic levels of type 3 (IL-6, TNFα,
620 IL17A, GMCSF), type 2 (IL-5) and T-cell inducing cytokines (IL-12p40, IL-12p70, IL-23) between
621 chow-fed (grey) and chronic HFD-fed WT (dark red) and *Tcrb-/-* (red) mice. Data are presented
622 as min – max values and median box plots. Box plot statistical analysis was performed by ANOVA
623 and Tukey post-hoc test.

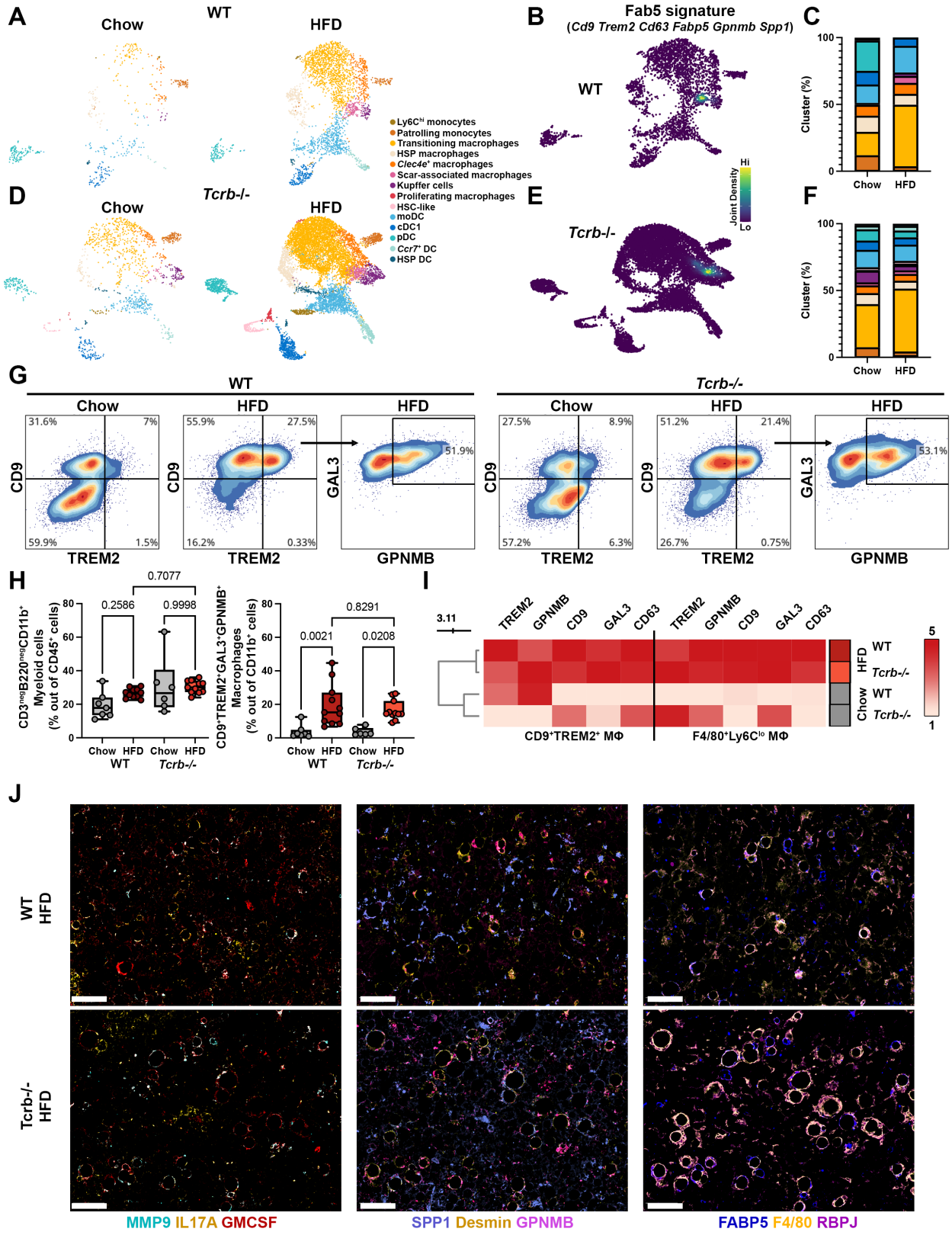
A
Chow
WT
HFD
Ly6C^hi monocytes
Patrolling monocytes
Transitioning macrophages
HSP macrophages
Clec4e+ macrophages
Scar-associated macrophages
Kupffer cells
Proliferating macrophages
HSC-like
moDC
cDC1
pDC
Ccr7+ DC
HSP DC
D
Chow
Tcrb-/-
HFD
B
Fab5 signature
(Cd9 Trem2 Cd63 Fabp5 Gpnmb Spp1)
WT
Tcrb-/-
Joint Density
Hi
Lo
E
C
Cluster (%)
100
50
0
Chow
HFD
F
G
WT
Tcrb-/-
Chow
HFD
HFD
31.6%
7%
59.9%
1.5%
55.9%
27.5%
16.2%
0.33%
51.9%
27.5%
8.9%
57.2%
6.3%
51.2%
21.4%
26.7%
0.75%
53.1%
CD9
TREM2
GAL3
GPNMB
H
CD3^neg B220^neg CD11b^+ Myeloid cells (% out of CD45^+ cells)
0.2586
0.9998
0.7077
CD9^+TREM2^+GAL3^+GPNMB^+ Macrophages (% out of CD11b^+ cells)
0.0021
0.0208
0.8291
Chow HFD Chow HFD
WT
Tcrb-/-
I
3.11
TREM2
GPNMB
CD9
GAL3
CD63
CD9^+TREM2^+ MΦ
F4/80^+Ly6C^lo MΦ
HFD
Chow
WT
Tcrb-/-
5
1
J
WT HFD
Tcrb-/- HFD
MMP9 IL17A GMCSF
SPP1 Desmin GPNMB
FABP5 F4/80 RBPJ

624

625 **Figure 7. SPP1^{+} scar-associated macrophages (SAMs) accumulate and persist in fibrosis,**
626 **independently of conventional CD8 T cells.**
627 (A,D) UMAP visualization of myeloid cells from livers of WT (A) and *Tcrb-/-* (D) mice after 40
628 weeks of chow (left) or HFD (right) by scRNA-seq. (B,E) Joint density expression of the pro-fibrotic
629 Fab5 signature (*Spp1, Gpnmb, Fabp5, Cd63, Cd9*) in WT (B) and *Tcrb-/-* (E) mice. (C,F) Stacked
630 bar chart showing the frequency of myeloid cell clusters between chow and HFD WT (C) and
631 *Tcrb-/-* (F) mice after 40 weeks. (G) Representative FACS plots showing the identification of
632 SPP1^{+} SAMs by flow cytometry using co-expression of CD9, TREM2, Galectin-3 and GPNMB in
633 F4/80^{+}Ly6C^{lo} macrophages from WT (left) and *Tcrb-/-* (right) mice. (H) Box plots showing the
634 relative frequency of myeloid cells from CD45^{+} cells (left) and the relative frequency of
635 CD9^{+}TREM2^{+}Galectin-3^{+}GPNMB^{+} SAMs from CD11b^{+} cells (right) between WT and *Tcrb-/-* mice
636 after 40 weeks on either chow or HFD. (I) Clustered heatmap showing the log2FC (scaled from 1
637 to 5) expression of scar-associated markers on F4/80^{+}Ly6C^{lo} or F4/80^{+}Ly6C^{lo}CD9^{+}TREM2^{lo}
638 macrophages between WT and *Tcrb-/-* mice at 40 weeks on either chow or chronic HFD. (J)
639 Representative immunofluorescent images from WT and *Tcrb-/-* mice after 40 weeks of HFD: left
640 panel for MMP9 (cyan), IL17A (yellow) and GMCSF (red), middle panel for SPP1 (light blue),
641 Desmin (yellow) and GPNMB (pink) and right panel for FABP5 (blue), F4/80 (yellow) and RBPJ
642 (magenta). Data are presented as min – max values and median box plots. Box plot statistical
643 analysis was performed by ANOVA and Tukey post-hoc test.
644

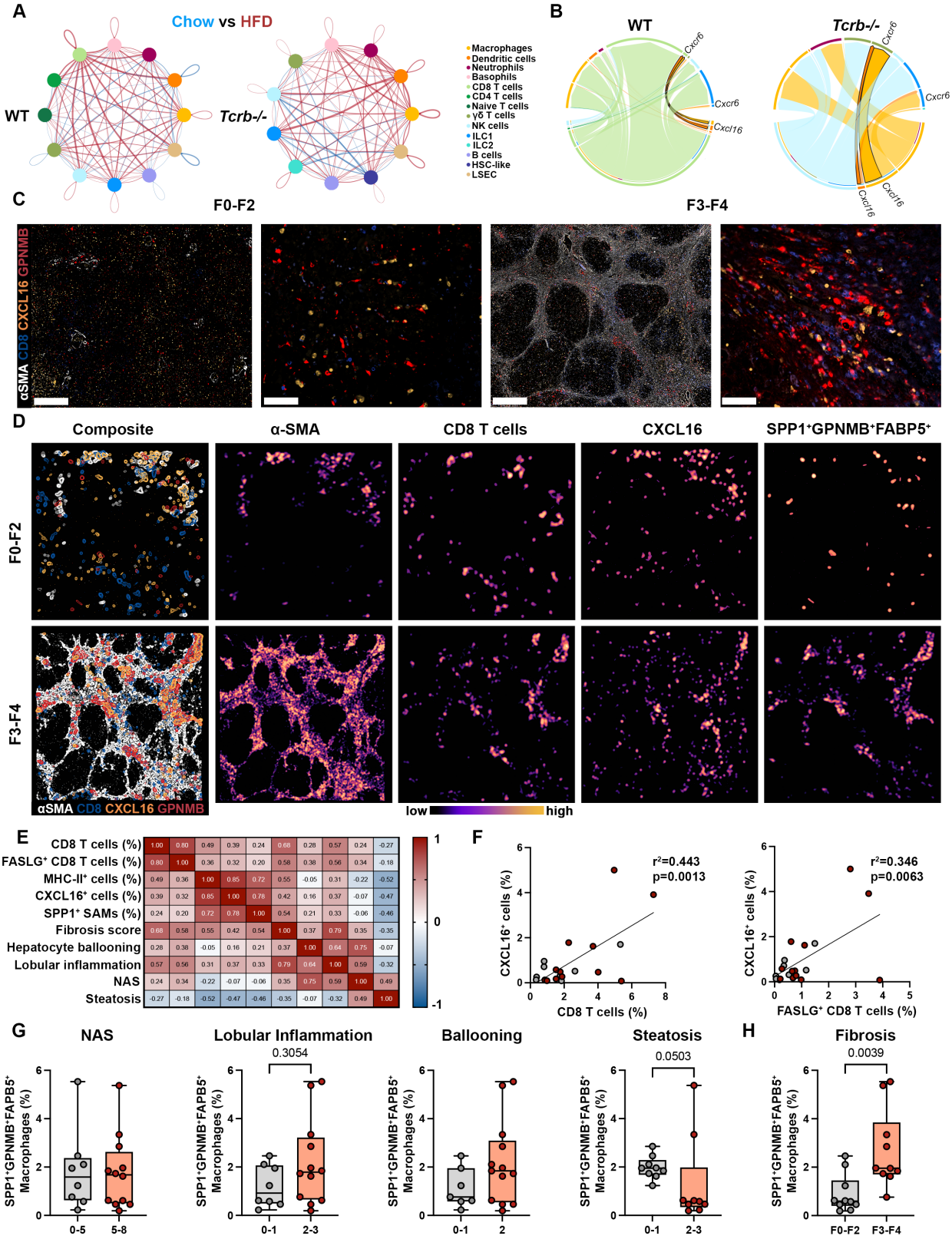
A
Chow vs HFD
WT
Tcrb-/-
Macrophages
Dendritic cells
Neutrophils
Basophils
CD8 T cells
CD4 T cells
Naive T cells
γδ T cells
NK cells
ILC1
ILC2
B cells
HSC-like
LSEC
B
WT
Tcrb-/-
Cxcr6
Cxcl16
C
F0-F2
F3-F4
αSMA CD8 CXCL16 GPNMB
D
Composite
α-SMA
CD8 T cells
CXCL16
SPP1⁺GPNMB⁺FABP5⁺
F0-F2
F3-F4
low
high
E
CD8 T cells (%)
FASLG⁺ CD8 T cells (%)
MHC-II⁺ cells (%)
CXCL16⁺ cells (%)
SPP1⁺ SAMs (%)
Fibrosis score
Hepatocyte ballooning
Lobular inflammation
NAS
Steatosis
F
r²=0.443
p=0.0013
CXCL16⁺ cells (%)
CD8 T cells (%)
r²=0.346
p=0.0063
FASLG⁺ CD8 T cells (%)
G
NAS
Lobular Inflammation
0.3054
Ballooning
Steatosis
0.0503
H
Fibrosis
0.0039
SPP1⁺GPNMB⁺FAPB5⁺ Macrophages (%)
0-5
5-8
0-1
2-3
2
F0-F2
F3-F4

645

646

647 **Figure 8. Myeloid cell expression of CXCL16 recruits CXCR6$^+$ T cells to the scar.**

648 (A) Circle plot showing the differential number of interactions between chow (blue) and HFD (red)
649 in WT (left) and *Tcrb-/-* (right) mice after 40 weeks by scRNA-seq. (B) Chord diagram visualizing
650 upregulated ligands mapped to their receptors in WT (left) and *Tcrb-/-* (right) mice. Black outline
651 highlights interactions between myeloid *Cxcl16* and conventional as well as γδ T cell *Cxcr6*
652 relative expression by scRNA-seq. (C) Representative immunofluorescent images of α-SMA
653 (white), CD8 (blue), CXCL16 (orange) and GPNMB (red) from F0-F2 (left) and F3-F4 (right) MASH
654 livers. (D) cycIF representative images showing the overlaid composite density of α-SMA (white),
655 CD8 (blue), CXCL16 (orange) and GPNMB (red) and the relative density of cells positive for α-
656 SMA, CD8, CXCL16, and GPNMB. (E) Heatmap showing spearman correlation (-1 to 1) between
657 the frequencies of CD8 T cells, FASLG$^+$ CD8 T cells, CXCL16$^+$ cells, MHC-II$^+$ cells, SPP1$^+$ SAMs,
658 fibrosis, hepatocyte ballooning, lobular inflammation, NAS and steatosis. (F) Spearman
659 correlation between the frequency of CXCL16$^+$ cells and the frequency of CD8 T cells (left) or
660 FASLG$^+$ CD8 T cells (right) in MASH livers. (G-H) Box plots showing the frequency of
661 SPP1$^+$GPNMB$^+$FABP5$^+$ SAMs with NAS, lobular inflammation, ballooning, steatosis (G) and
662 fibrosis (H). Data are presented as min – max values and median box plots. Box plot statistical
663 analysis was performed by Mann-Whitney test.

Figure S1

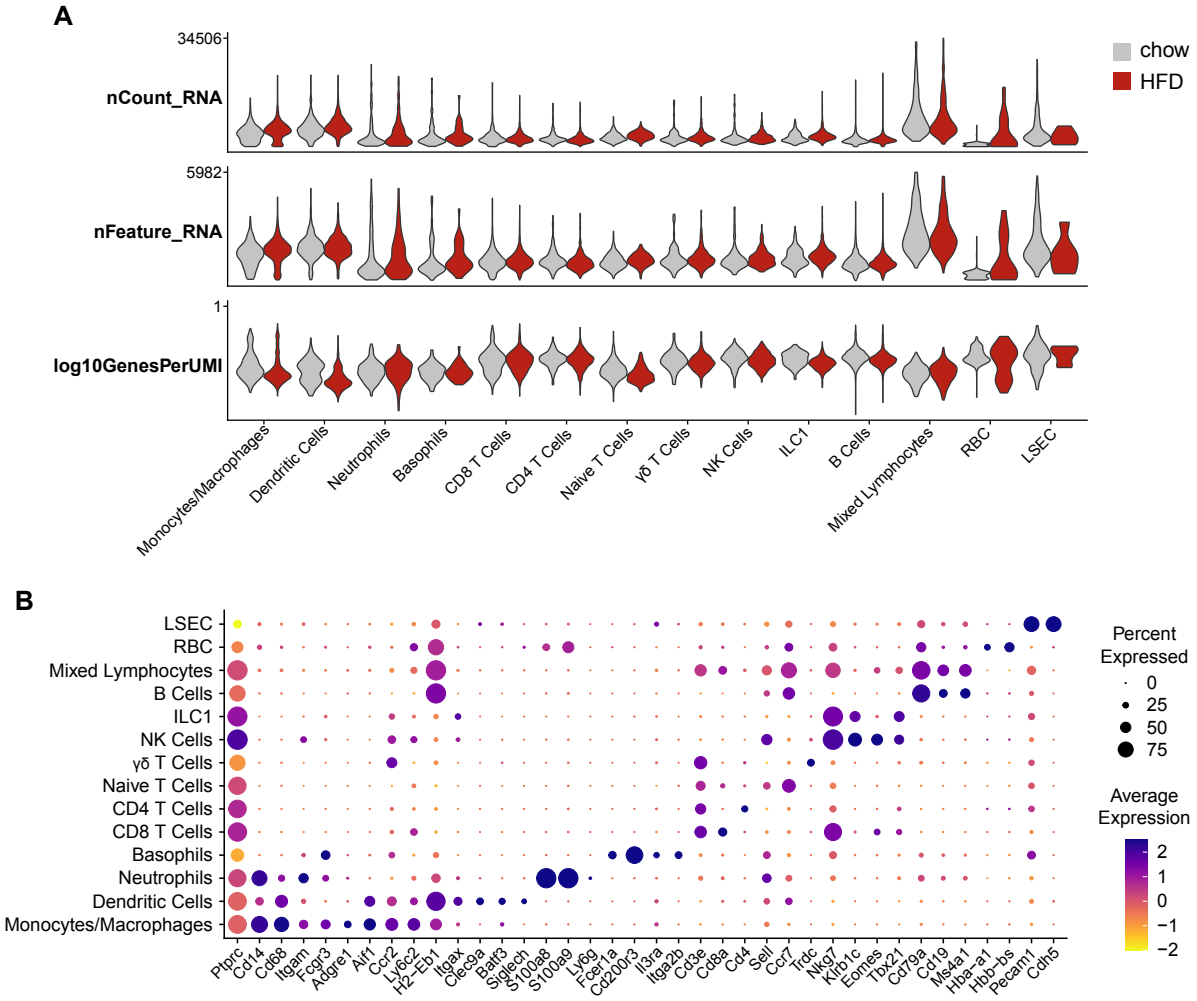

Supplementary Figure 1. Livers of chow- and HFD-fed wild-type (WT) mice profiled by scRNA-seq.

(A) Stacked violin plots of UMI, gene expression, and cell complexity by cell type in chow (grey) and HFD-fed (red) WT mice after 40 weeks of diet. (B) Dot plot of global marker gene expression in chow and HFD-fed WT mice combined.

Figure S2

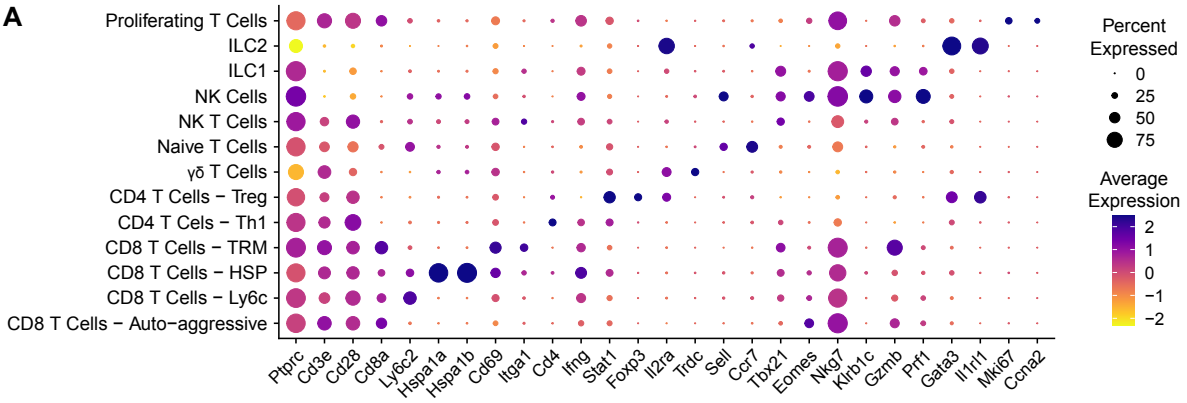

Supplementary Figure 2. WT liver lymphocyte gene expression by scRNA-seq.

(A) Dot plot of marker gene expression in subclustered lymphocytes from livers of chow and HFD-fed WT mice combined.

Figure S3

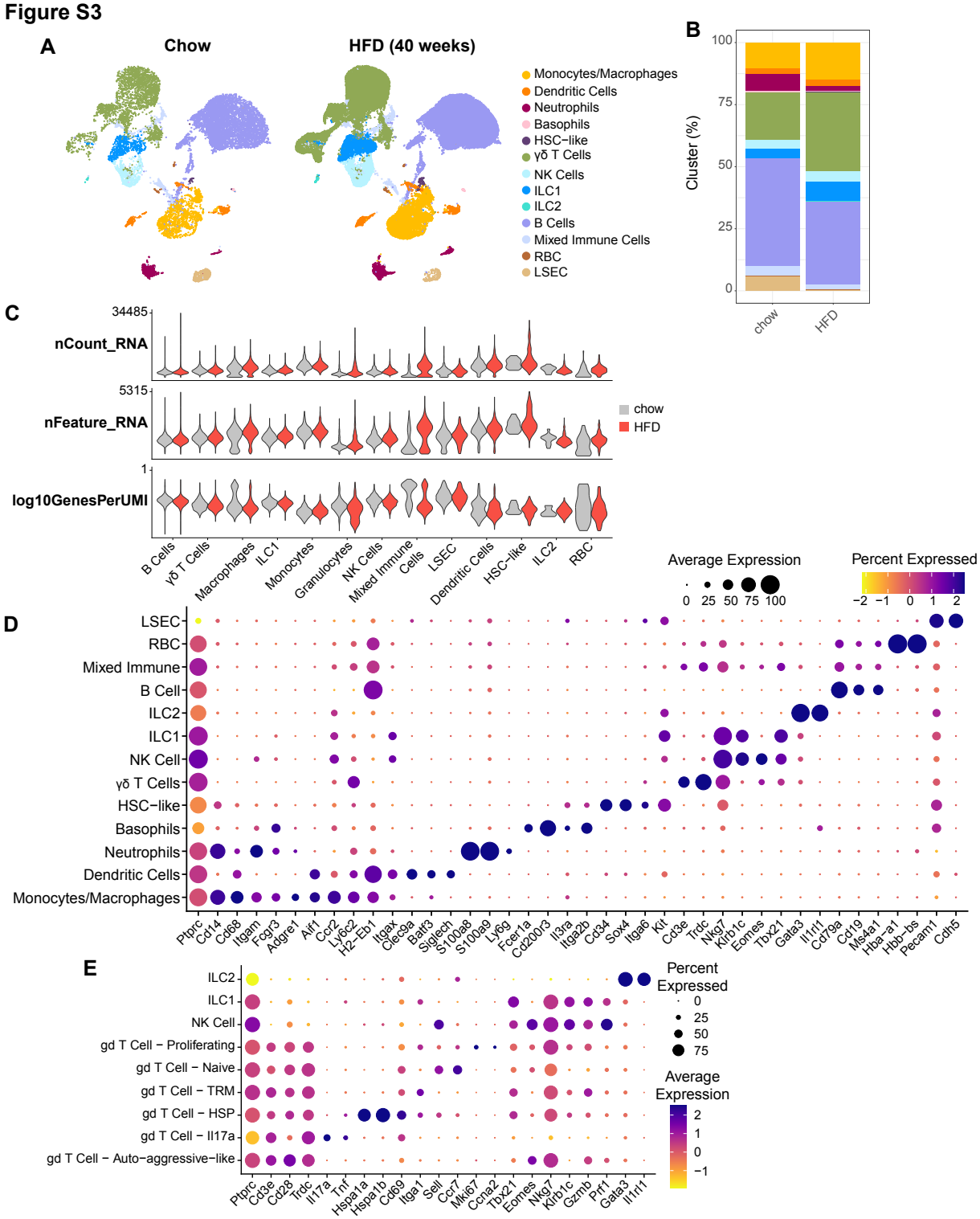

674

675

676

677 **Supplementary Figure 3. Livers of chow- and HFD-fed *Tcrb*$^{-/-}$ mice profiled by scRNA-seq.**
678 (A) Split UMAP of scRNA-seq global cell annotations from chow and HFD-fed *Tcrb*-/- mice after
679 40 weeks of diet. (B) Relative abundancies of global populations detected by scRNA-seq. (C)
680 Stacked violin plots of UMI, gene expression, and cell complexity by cell type in chow (grey) and
681 HFD-fed (red) *Tcrb*-/- mice. (D-E) Dot plots of global (D) and lymphocyte (E) marker gene
682 expression in livers of chow- and HFD-fed *Tcrb*-/- mice combined.

Figure S4

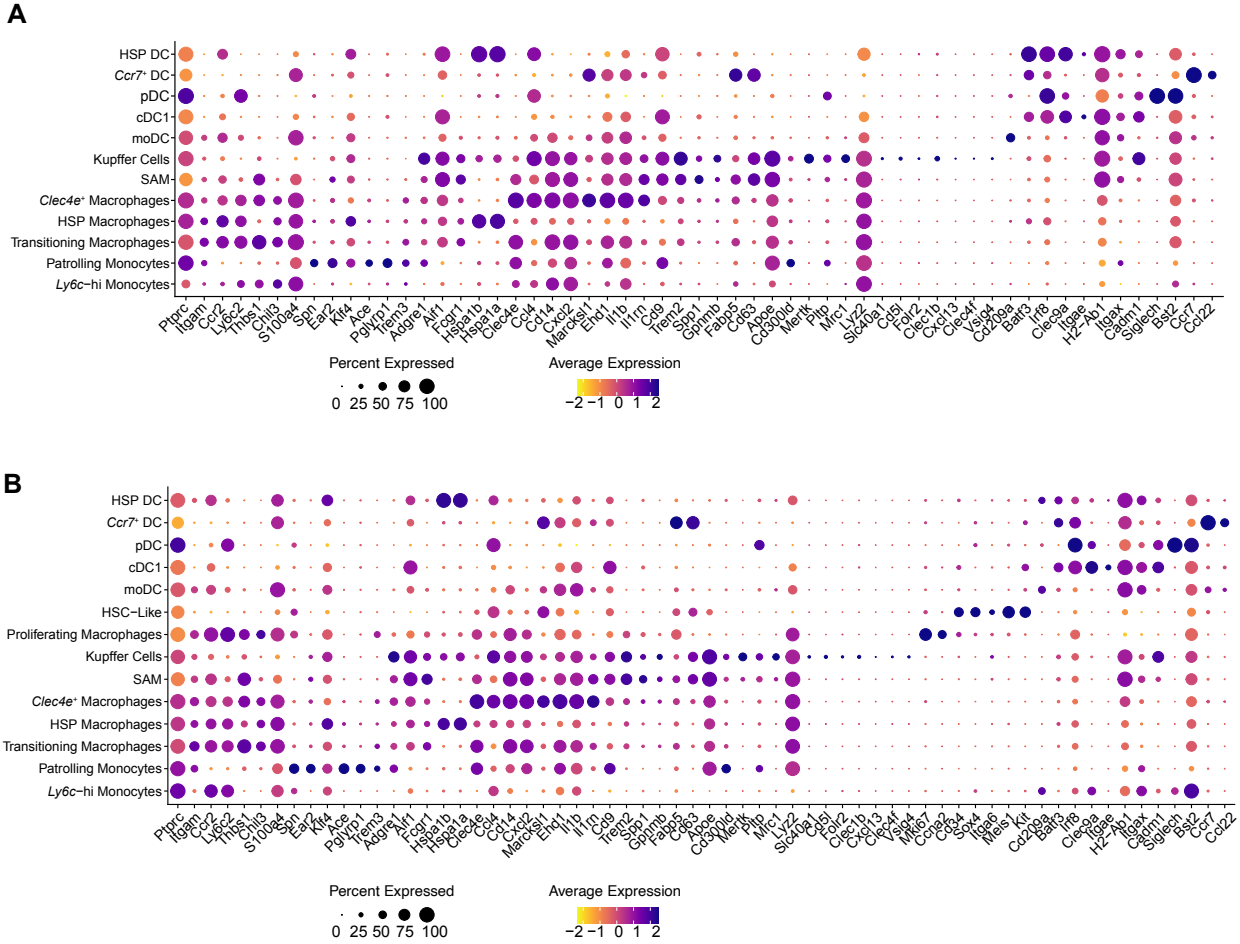

683

684 **Supplementary Figure 4. MASH liver myeloid gene expression by scRNA-seq.**

685 Dot plots of marker gene expression in combined chow- and HFD-fed WT mice (A) and *Tcrb*-/-

686 mice (B).

Figure S5

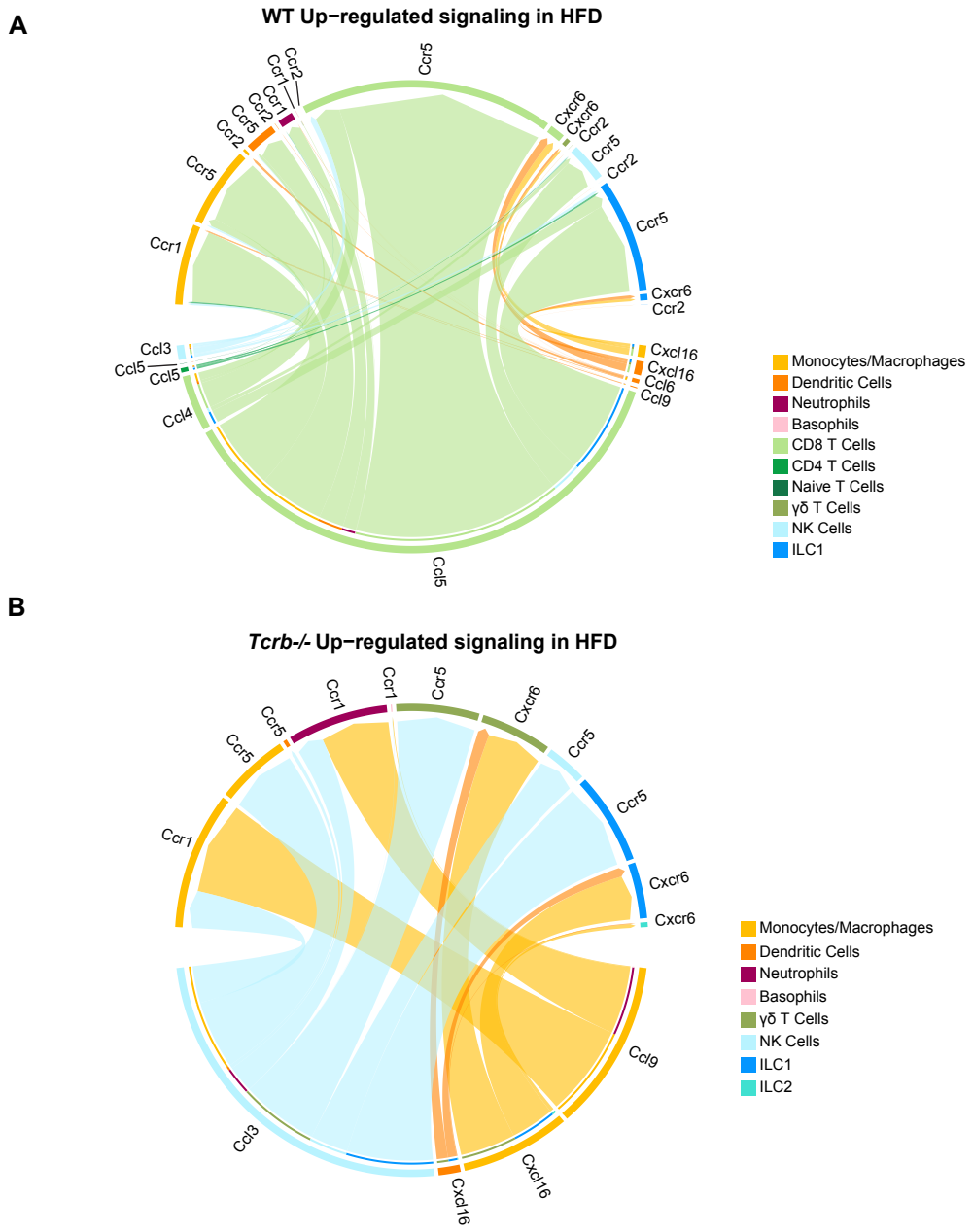

Supplementary Figure 5. MASH liver chemokine/receptor interaction predictions from scRNA-seq.

Interactions upregulated in livers of HFD-fed WT (A) and *Tcrb-/-* (B) compared to chow-fed mice.

691 **Table S1. Patient metadata**

Patient ID	Disease	Fibrosis Stage	Hepatocyte Ballooning	Lobular Inflammation	NAS	Steatosis
F202288354388482	MASLD/MASH	4	1	1	3	1
F269667491781714	MASLD/MASH	1	2	2	7	3
F25230374217327	MASLD/MASH	3	0	3	3	0
F60076066942084	MASLD/MASH	4	2	3	6	1
F93815000985241	MASLD/MASH	4	2	3	6	1
F164630764073724	MASLD/MASH	0	0	1	3	2
F18870497925578	MASLD/MASH	3	1	2	3	0
F54808383304812	MASLD/MASH	2	2	2	7	3
F89655557507529	MASLD/MASH	4	2	3	5	0
F160333745451172	MASLD/MASH	0	0	1	3	2
F194072749341725	MASLD/MASH	4	2	3	8	3
F228919843573023	MASLD/MASH	4	2	3	5	0
F17160862857391	MASLD/MASH	4	2	3	5	0
F51999294867643	MASLD/MASH	3	2	3	7	2
F89045601851397	MASLD/MASH	2	2	3	7	2
F224751406165187	MASLD/MASH	0	2	1	3	0
F12855615291317	MASLD/MASH	1	1	1	5	3
F47702485095320	MASLD/MASH	1	1	1	3	1
F82540773355965	MASLD/MASH	0	1	1	5	3
F118489267437699	MASLD/MASH	1	1	1	4	2

692

693 **Table S2. Flow cytometry antibodies**

Target	Fluorophore	Clone	Panel
Trem2	FITC	78.18	SAMs
CD45	A700	30-F11	SAMs
GPNMB	e660	CTSREVL	SAMs
CD9	APC-Fire750	MZ3	SAMs
CD3	BUV395	145-2C11	SAMs
B220	BUV395	RA3-6B2	SAMs
Siglec-F	BUV395	E50-2440	SAMs
NK1.1	BUV395	PK-136	SAMs
CD11b	BUV787	M1/70	SAMs
CD81	BV421	EAT2	SAMs
F4/80	BV605	T45-2342	SAMs
Galectin-3	PE	M3/38	SAMs
Ly6G	PE-CF594	1A8	SAMs
Ly6C	PECy7	HK1.4	SAMs
CD63	PerCP.Cy5.5	NVG2	SAMs
Galectin-3	PE	M3/38	SAMs
Ly6G	PE-CF594	1A8	SAMs
Ly6C	PE-Cy7	HK1.4	SAMs
F4/80	BB515	T45-2342	Lineage
CD11c	PerCP.Cy5.5	N418	Lineage
TCRgd	BV421	GL3	Lineage
CD11b	BV605	M1/70	Lineage
B220	BV786	RA3-6B2	Lineage
CD3	BUV395	145-2C11	Lineage
CD4	BUV496	GK1.5	Lineage
CD8	BUV787	53-6.7	Lineage
CD68	APC	FA-11	Lineage
CD45	A700	30-F11	Lineage
NK1.1	APC-Cy7	PK-136	Lineage
Siglec-F	PE	E50-2440	Lineage
Ly6G	PE-CF584	1A8	Lineage
Ly6C	PE-Cy7	HK1.4	Lineage
CD44	A488	KM81	CD8 T cell
CD45	A700	30-F11	CD8 T cell
FASL	APC	MFL3	CD8 T cell
CD62L	APC-Cy7	MEL-14	CD8 T cell
CD3	BUV395	145-2C11	CD8 T cell

CD4	BUV496	GK1.5	CD8 T cell
CD8	BUV787	53-6.7	CD8 T cell
PD1	BV421	J43	CD8 T cell
CD69	BV605	H1-2F3	CD8 T cell
Tbet	BV785	O4-46	CD8 T cell
Eomes	PE	X4-83	CD8 T cell
CD103	PE-CF594	M290	CD8 T cell
CXCR6	PE-Cy7	SA051D1	CD8 T cell
Tim-3	PerCP-CY5.5	RMT3-23	CD8 T cell

694

695 **Table S3. Human cycIF antibodies**

Antibody	Catalog #	Company	Isotype	Clone
CD3e	MA5-16622	ThermoFisher Scientific	Rat	cd3-12
CD8a	NBP2-32836	Novus Biologicals	Mouse	C8/114B
Tim-3	AF2365	R&D	Goat	pAb
PD-1	367402	Biolegend	Mouse	NAT105
CXCL16	AF976	R&D Systems	Goat	pAb
FasLG	BS-0216R	Bioss	Rabbit	pAb
IL-17	AF-317-NA	R&D Systems	Goat	pAb
FABP5	MAB3077	R&D Systems	Rat	311215
PD-1	367402	Biolegend	Mouse	NAT105
Smooth muscle actin (SMA)	MAB1420	R&D Systems	Mouse	1A4
GPNMB/Osteoactivin	AF2550	R&D Systems	Goat	pAb
CD63	ab134045	Abcam	Rabbit	EPR5702
Galectin 3	NBP2-16589	Novus	Rabbit	pAb
Spp1/Osteopontin	AF1433	R&D Systems	Goat	pAb
PD-L1	AF156	R&D Systems	Goat	pAb
HLA-DR	NBP2-53380	Novus Biologicals	Mouse	CR3/43
CD248	379102	Biolegend	Mouse	B1/35
Desmin	PA5-16705	ThermoFisher Scientific	Rabbit	pAb
Podoplanin	AF3670	R&D Systems	Sheep	pAb

696

697 **Table S4. Mouse cycIF antibodies**

Antibody	Catalog #	Company	Isotype	Clone
S100A8/9	NBP2-27067	Novus	Rat	63N13G5
FABP5	AF1476	R&D Systems	Goat	pAb
IL-17A	PAA063Mu01	Cloud-Clone Corp	Rabbit	pAb
GMCSF	PAA045Mu01	Cloud-Clone Corp	RAbbit	pAb
MMP9	AF909	R&D Systems	Goat	pAb
IBA1	PA5-143572	ThermoFisher Scientific	Chicken	pAb
SPP1	AF808	R&D Systems	Goat	pAb
GPNMB	NBP1-69389	R&D Systems	Rabbit	pAb
Desmin	PA5-85187	ThermoFisher Scientific	Rabbit	pAb
Galectin-3	AF1197	R&D Systems	Goat	pAb
Clec4f	AF2784	R&D Systems	Goat	pAb
F4/80	70076	Cell Signaling Technology	Rabbit	D2S9R
RBPJ	5313	Cell Signaling Technology	Rabbit	D10A4
CD206	AF2335	R&D Systems	Goat	pAb

698

699 **Abbreviations**

700 CCl_4, carbon tetrachloride

701 CDA, choline-deficient diet

702 CDHFD, choline-deficient high-fat diet

703 CPM, counts per million

704 cycIF, cyclic immunofluorescence

705 DC, dendritic cell

706 DMN, dimethylnitrosamine

707 ECM, extracellular matrix

708 FACS, fluorescence-activated cell sorting

709 FBS, fetal bovine serum

710 FFPE, formalin-fixed paraffin-embedded

711 HBV and HCV, hepatitis B virus and hepatitis C virus, respectively

712 HFD, high-fat diet

713 HSC, hepatic stellate cell

714 IF, immunofluorescence

715 IHL, intrahepatic leukocyte

716 MASLD, metabolic dysfunction-associated steatotic liver disease

717 MASH, metabolic dysfunction-associated steatohepatitis

718 MCDD, methionine and choline-deficient diet

719 MDM, monocyte-derived macrophage

720 NAFLD, non-alcoholic fatty liver disease (*now referred to as MASLD*)

721 NAS, NAFLD activity score

722 NASH, non-alcoholic steatohepatitis (*now referred to as MASH*)

723 PBS, phosphate buffered saline

724 SAM, scar-associated macrophage

725 scRNA-seq, single cell RNA-seq

726 TRM, tissue-resident macrophage

727 WT, wild-type

728

729 **Financial support**

730 This study was financed by Pfizer Inc.

731

732 **Conflict of interest**

733 C.L, K.L.D., S.L., S.M.C., S.A., M.H.W., K.B., S.D., T.A.W., K.M.H., T.F. are or J.M., F.S., C.W.,

734 X.C., A.M.S.B. were employees of Pfizer Inc.

735

736 **Author contributions**

737 Acquisition, analysis and interpretation of data: C.L, K.L.D., S.L., S.M.C., S.A., M.H.W., K.B, S.D.,

738 J.M., F.S., C.W., X.C., A.M.S.B., K.M.H., T.F. Drafting and writing of the manuscript: C.L., K.L.D,

739 T.F. Critical revision of the manuscript for important intellectual content: T.A.W. Study concept,

740 design supervision: A.M.S.B., T.A.W., K.M.H., T.F.

741

742 **Data availability**

743 The datasets generated and/or analyzed during the present study are available from the

744 corresponding author upon reasonable, scientifically justified request.

745

746 **Acknowledgements**

747 We thank the Pfizer Flow Cytometry, Optical Microscopy, High Content Imaging, and Next-

748 Generation Sequencing Technology Centers. K.L.D. thanks the Pfizer Postdoctoral Fellowship

749 Program for support.

750 **References**

751 1 Le, P. *et al.* Estimated Burden of Metabolic Dysfunction-Associated Steatotic Liver
752 Disease in US Adults, 2020 to 2050. *JAMA Netw Open* **8**, e2454707,
753 doi:10.1001/jamanetworkopen.2024.54707 (2025).
754 2 Xiang, L. *et al.* Safety and efficacy of GLP-1/FGF21 dual agonist HEC88473 in MASLD
755 and T2DM: A randomized, double-blind, placebo-controlled study. *J Hepatol* **82**, 967-978,
756 doi:10.1016/j.jhep.2024.12.006 (2025).
757 3 Sanyal, A. J. *et al.* Phase 3 Trial of Semaglutide in Metabolic Dysfunction-Associated
758 Steatohepatitis. *N Engl J Med* **392**, 2089-2099, doi:10.1056/NEJMoa2413258 (2025).
759 4 Hammerich, L. & Tacke, F. Hepatic inflammatory responses in liver fibrosis. *Nat Rev*
760 *Gastroenterol Hepatol* **20**, 633-646, doi:10.1038/s41575-023-00807-x (2023).
761 5 Foster, R. G., Golden-Mason, L., Rutebemberwa, A. & Rosen, H. R. Interleukin (IL)-17/IL-
762 22-producing T cells enriched within the liver of patients with chronic hepatitis C viral
763 (HCV) infection. *Dig Dis Sci* **57**, 381-389, doi:10.1007/s10620-011-1997-z (2012).
764 6 Li, J. *et al.* Significance of the balance between regulatory T (Treg) and T helper 17 (Th17)
765 cells during hepatitis B virus related liver fibrosis. *PLoS One* **7**, e39307,
766 doi:10.1371/journal.pone.0039307 (2012).
767 7 Zhao, L. *et al.* Interleukin-17 contributes to the pathogenesis of autoimmune hepatitis
768 through inducing hepatic interleukin-6 expression. *PLoS One* **6**, e18909,
769 doi:10.1371/journal.pone.0018909 (2011).
770 8 Claassen, M. A., de Knegt, R. J., Tilanus, H. W., Janssen, H. L. & Boonstra, A. Abundant
771 numbers of regulatory T cells localize to the liver of chronic hepatitis C infected patients
772 and limit the extent of fibrosis. *J Hepatol* **52**, 315-321, doi:10.1016/j.jhep.2009.12.013
773 (2010).
774 9 Wasmuth, H. E. *et al.* Antifibrotic effects of CXCL9 and its receptor CXCR3 in livers of
775 mice and humans. *Gastroenterology* **137**, 309-319, 319 e301-303,
776 doi:10.1053/j.gastro.2009.03.053 (2009).
777 10 Teixeira, R., Marcos, L. A. & Friedman, S. L. Immunopathogenesis of hepatitis C virus
778 infection and hepatic fibrosis: New insights into antifibrotic therapy in chronic hepatitis C.
779 *Hepatol Res* **37**, 579-595, doi:10.1111/j.1872-034X.2007.00085.x (2007).
780 11 Fabre, T. *et al.* Type 3 cytokines IL-17A and IL-22 drive TGF-beta-dependent liver fibrosis.
781 *Sci Immunol* **3**, doi:10.1126/sciimmunol.aar7754 (2018).
782 12 Rong, G. *et al.* Imbalance between T helper type 17 and T regulatory cells in patients with
783 primary biliary cirrhosis: the serum cytokine profile and peripheral cell population. *Clin Exp*
784 *Immunol* **156**, 217-225, doi:10.1111/j.1365-2249.2009.03898.x (2009).
785 13 Ichiki, Y. *et al.* T cell immunity in autoimmune hepatitis. *Autoimmun Rev* **4**, 315-321,
786 doi:10.1016/j.autrev.2005.01.005 (2005).
787 14 Russell, J. Q. *et al.* Liver damage preferentially results from CD8(+) T cells triggered by
788 high affinity peptide antigens. *J Exp Med* **188**, 1147-1157, doi:10.1084/jem.188.6.1147
789 (1998).
790 15 Shi, Z., Wakil, A. E. & Rockey, D. C. Strain-specific differences in mouse hepatic wound
791 healing are mediated by divergent T helper cytokine responses. *Proc Natl Acad Sci U S A*
792 **94**, 10663-10668, doi:10.1073/pnas.94.20.10663 (1997).
793 16 Hyon, M. K., Kwon, E., Choi, H. J. & Kang, B. C. Dimethylnitrosamine-induced liver fibrosis
794 and recovery in NOD/SCID mice. *J Vet Med Sci* **73**, 739-745, doi:10.1292/jvms.10-0311
795 (2011).
796 17 Hernandez-Gea, V. & Friedman, S. L. Pathogenesis of liver fibrosis. *Annu Rev Pathol* **6**,
797 425-456, doi:10.1146/annurev-pathol-011110-130246 (2011).
798 18 Hart KM, F. T., Sciurba JS, Gieseck RL III, Borthwick LA, Vannella KM, Acciani TH, de
799 Queiroz Prado R, Thompson RW, White S, Soucy G, Bilodeau M, Ramalingam TR,

Shoukry NH, and Wynn TA. Type-2 immunity is protective in metabolic disease but exacerbates NAFLD collaboratively with TGF-β. *Sci Transl Med* **In press** (2017).

19 Wolf, M. J. *et al.* Metabolic activation of intrahepatic CD8+ T cells and NKT cells causes nonalcoholic steatohepatitis and liver cancer via cross-talk with hepatocytes. *Cancer Cell* **26**, 549-564, doi:10.1016/j.ccell.2014.09.003 (2014).

20 Deczkowska, A. *et al.* XCR1(+) type 1 conventional dendritic cells drive liver pathology in non-alcoholic steatohepatitis. *Nat Med* **27**, 1043-1054, doi:10.1038/s41591-021-01344-3 (2021).

21 Dudek, M. *et al.* Auto-aggressive CXCR6(+) CD8 T cells cause liver immune pathology in NASH. *Nature* **592**, 444-449, doi:10.1038/s41586-021-03233-8 (2021).

22 Flores Molina, M. *et al.* Visualization, Quantification, and Mapping of Immune Cell Populations in the Tumor Microenvironment. *J Vis Exp*, doi:10.3791/60740 (2020).

23 Fabre, T. *et al.* Identification of a broadly fibrogenic macrophage subset induced by type 3 inflammation. *Sci Immunol* **8**, eadd8945, doi:10.1126/sciimmunol.add8945 (2023).

24 Schindelin, J. *et al.* Fiji: an open-source platform for biological-image analysis. *Nat Methods* **9**, 676-682, doi:10.1038/nmeth.2019 (2012).

25 Botvinik-Nezer, R. *et al.* Variability in the analysis of a single neuroimaging dataset by many teams. *Nature* **582**, 84-88, doi:10.1038/s41586-020-2314-9 (2020).

26 McGinnis, C. S. *et al.* MULTI-seq: sample multiplexing for single-cell RNA sequencing using lipid-tagged indices. *Nat Methods* **16**, 619-626, doi:10.1038/s41592-019-0433-8 (2019).

27 Hao, Y. *et al.* Dictionary learning for integrative, multimodal and scalable single-cell analysis. *Nat Biotechnol* **42**, 293-304, doi:10.1038/s41587-023-01767-y (2024).

28 Young, M. D. & Behjati, S. SoupX removes ambient RNA contamination from droplet-based single-cell RNA sequencing data. *Gigascience* **9**, doi:10.1093/gigascience/giaa151 (2020).

29 Stoeckius, M. *et al.* Cell Hashing with barcoded antibodies enables multiplexing and doublet detection for single cell genomics. *Genome Biol* **19**, 224, doi:10.1186/s13059-018-1603-1 (2018).

30 Hafemeister, C. & Satija, R. Normalization and variance stabilization of single-cell RNA-seq data using regularized negative binomial regression. *Genome Biol* **20**, 296, doi:10.1186/s13059-019-1874-1 (2019).

31 Alquicira-Hernandez, J. & Powell, J. E. Nebulosa recovers single-cell gene expression signals by kernel density estimation. *Bioinformatics* **37**, 2485-2487, doi:10.1093/bioinformatics/btab003 (2021).

32 Butler, A., Hoffman, P., Smibert, P., Papalexi, E. & Satija, R. Integrating single-cell transcriptomic data across different conditions, technologies, and species. *Nat Biotechnol* **36**, 411-420, doi:10.1038/nbt.4096 (2018).

33 Chu, T., Wang, Z., Pe'er, D. & Danko, C. G. Cell type and gene expression deconvolution with BayesPrism enables Bayesian integrative analysis across bulk and single-cell RNA sequencing in oncology. *Nat Cancer* **3**, 505-517, doi:10.1038/s43018-022-00356-3 (2022).

34 Love, M. I., Huber, W. & Anders, S. Moderated estimation of fold change and dispersion for RNA-seq data with DESeq2. *Genome Biol* **15**, 550, doi:10.1186/s13059-014-0550-8 (2014).

35 Carenzo, A. *et al.* hacksig: a unified and tidy R framework to easily compute gene expression signature scores. *Bioinformatics* **38**, 2940-2942, doi:10.1093/bioinformatics/btac161 (2022).

36 Satija, R., Farrell, J. A., Gennert, D., Schier, A. F. & Regev, A. Spatial reconstruction of single-cell gene expression data. *Nat Biotechnol* **33**, 495-502, doi:10.1038/nbt.3192 (2015).

37 Govaere, O. *et al.* Transcriptomic profiling across the nonalcoholic fatty liver disease spectrum reveals gene signatures for steatohepatitis and fibrosis. *Sci Transl Med* **12**, doi:10.1126/scitranslmed.aba4448 (2020).
38 Vacca, M. *et al.* An unbiased ranking of murine dietary models based on their proximity to human metabolic dysfunction-associated steatotic liver disease (MASLD). *Nat Metab* **6**, 1178-1196, doi:10.1038/s42255-024-01043-6 (2024).
39 Guo, W. *et al.* Notch signaling regulates macrophage-mediated inflammation in metabolic dysfunction-associated steatotic liver disease. *Immunity* **57**, 2310-2327 e2316, doi:10.1016/j.immuni.2024.08.016 (2024).
40 Burtis, A. E. C. *et al.* Ag-driven CD8 + T cell clonal expansion is a prominent feature of MASH in humans and mice. *Hepatology* **81**, 591-608, doi:10.1097/HEP.0000000000000971 (2025).
41 Dywicki, J. *et al.* From model to man: Understanding Tregs' dual role in MASLD. *JHEP Reports* **7**, doi:10.1016/j.jhepr.2025.101619 (2025).
42 Hammerich, L. & Tacke, F. Role of gamma-delta T cells in liver inflammation and fibrosis. *World J Gastrointest Pathophysiol* **5**, 107-113, doi:10.4291/wjgp.v5.i2.107 (2014).
43 Ma, H. Y. *et al.* IL-17 signaling in steatotic hepatocytes and macrophages promotes hepatocellular carcinoma in alcohol-related liver disease. *J Hepatol* **72**, 946-959, doi:10.1016/j.jhep.2019.12.016 (2020).
44 Kim, J. Y. *et al.* ER Stress Drives Lipogenesis and Steatohepatitis via Caspase-2 Activation of S1P. *Cell* **175**, 133-145 e115, doi:10.1016/j.cell.2018.08.020 (2018).
45 Fabre, T., Kared, H., Friedman, S. L. & Shoukry, N. H. IL-17A Enhances the Expression of Profibrotic Genes through Upregulation of the TGF-beta Receptor on Hepatic Stellate Cells in a JNK-Dependent Manner. *J Immunol* **193**, 3925-3933, doi:10.4049/jimmunol.1400861 (2014).
46 Wehr, A. *et al.* Pharmacological inhibition of the chemokine CXCL16 diminishes liver macrophage infiltration and steatohepatitis in chronic hepatic injury. *PLoS One* **9**, e112327, doi:10.1371/journal.pone.0112327 (2014).
47 Krenkel, O. *et al.* Therapeutic inhibition of inflammatory monocyte recruitment reduces steatohepatitis and liver fibrosis. *Hepatology* **67**, 1270-1283, doi:10.1002/hep.29544 (2018).
48 Lefebvre, E. *et al.* Antifibrotic Effects of the Dual CCR2/CCR5 Antagonist Cenicriviroc in Animal Models of Liver and Kidney Fibrosis. *PLoS One* **11**, e0158156, doi:10.1371/journal.pone.0158156 (2016).
49 Baeck, C. *et al.* Pharmacological inhibition of the chemokine CCL2 (MCP-1) diminishes liver macrophage infiltration and steatohepatitis in chronic hepatic injury. *Gut* **61**, 416-426, doi:10.1136/gutjnl-2011-300304 (2012).
50 Anstee, Q. M. *et al.* Tropifexor plus cenicriviroc combination versus monotherapy in nonalcoholic steatohepatitis: Results from the phase 2b TANDEM study. *Hepatology* **78**, 1223-1239, doi:10.1097/HEP.0000000000000439 (2023).